Techniques for Coherent Control of Effective Photon-Photon Interactions at Low Light Levels

by

Cameron Vickers

A thesis
presented to the University of Waterloo
in fulfillment of the
thesis requirement for the degree of
Master of Science
in
Physics (Quantum Information)

Waterloo, Ontario, Canada, 2019

Author's Declaration

I hereby declare that I am the sole author of this thesis. This is a true copy of the thesis, including any required final revisions, as accepted by my examiners.

I understand that my thesis may be made electronically available to the public.

Abstract

This thesis proposes improvements on techniques for the coherent control of photon-photon interactions mediated by a cloud of cold atoms. Atoms cooled and trapped in a MOT can be loaded into a hollow, photonic crystal waveguide to ensure light coupled into the waveguide is localized on the tightly confined atoms. The low temperature of the atoms decreases decoherence rates, and improves coherent light-matter interactions, such as electromagnetically induced transparency and slow light. Predictions are made for two future experiments using this system, modulating of the phase of a laser beam with a much weaker one, and modulating the transmission of a laser through two photon absorption. These predictions indicate that the phase of a $0.1\mu W$ laser beam can be modulated by as much as one milliradian per weak laser photon, and that a $800pW$ laser beam can modulate the transmission of a comparably powerful laser by as much as 60%. Both of these predictions would be improvements on results for similar experiments performed with warm atoms.

Acknowledgements

I would like to thank the many people who helped me to reach this point. My undergraduate and graduate advisors, William Stwalley and Michal Bajcsy, provided me with environments to explore the physical world, and taught me how to be an experimental physicist. I have had many great professors who gave me a strong foundation in quantum physics, and for this I would like to thank Thomas Blum and Peter Schewitzer at the University of Connecticut, and Jon Yard at the University of Waterloo. Lastly, I would like to thank my lab mates for supporting me, and helping me to become a better physicist. I thank Taehyun Yoon, Jeremy Flannery, Fereshteh Rajabi, and Rubayet Al Maruf for patiently demonstrating many essential laboratory techniques, and for always being willing to help me understand theory. I thank Sreesh Venuturumilli, Andy Ding, Jackson Qiu, Brian Duong, and Turner Silverhorne for the support and insights that they gave me. I wish you all success in your pursuit of knowledge, and look forward to meeting you again further on in our careers.

Dedication

I would like to dedicate this thesis to my partner, Maddie Gretzky, who has been immensely supporting in my aspirations to become an experimental physicist. I know I could not be where I am without her.

Table of Contents

List of Figures viii

1 Introduction 1

1.1 Motivation . . . 1
1.2 Two Level Atom . . . 3
1.3 Atomic Media . . . 7
1.4 Atomic Motion . . . 11
1.5 Three Level Atom of Ladder Type . . . 12
1.6 Three Level Atom of Λ Type and Electromagnetically Induced Transparency 15
1.7 Slow Light . . . 19

2 Effective Photon-Photon Interactions 21

2.1 Cross Phase Modulation . . . 22
2.2 Two Photon Absorption . . . 29

3 Experimental Design 33

3.1 Dichroic Atomic Vapor Laser Lock . . . 33
3.2 Main Experimental Setup . . . 38
3.3 Mach-Zehnder Interferometer . . . 41

4 Conclusion **45**

4.1 Summary 45

4.2 Future Work 46

References **49**

A Physical Constants **52**

B Lens Tipped Fibers **54**

C Laser Locking Circuit **61**

D Python Code **65**

E Mot Components **71**

List of Figures

1.1 (Top Left) Hollow Core Photonic Crystal Fiber, Thorlabs product HC-1550. (Top Right) Hollow core ARROW waveguide [17]. (Bottom) One dimensional photonic crystal wire [20] 3

1.2 Two level atom interacting with an electric field. The energy separation of the levels is $\hbar\omega_{21}$ 5

1.3 (Left) Probability of finding a two level atom in the excited state as a function of Δ/Γ for increasing Rabi frequencies, found from $\tilde{\rho}_{22}$ in Eq. 1.10 . It can be seen that the probability saturates at 50%, and further increases in Rabi frequency broaden the peak. (Right) Real and imaginary parts of $\tilde{\rho}_{21}$ from Eq. 1.10 for $\Omega = \Gamma/2$. As will be discussed in section 1.3, the real part determines the index of refraction of the atom as experienced by the field, and the imaginary part is proportional to the absorption coefficient of the atom. 6

1.4 (Left) Transmission of light through a one centimeter length cloud of two level atoms for several optical depths and $\Omega = \Gamma$. (Right) Absorption length for an atomic cloud with optical depth of one hundred and varied Rabi frequencies. 9

1.5 Imaginary (left) and real (right) parts of the susceptibility of an ensemble of two level atoms at several temperatures. Higher temperatures reduce and broaden features near resonance, though off resonant behavior remains nearly the same. Horizontal black lines mark zero 12

1.6 Three level Cascade scheme 13

1.7 Comparison of density matrix element ρ_{22} calculated by numerically solving the master equation (solid line) and the stochastic wavefunction approach in the weak probe field limit (dashed line), for $\Delta_{32} = 0$ and $\Omega_{32} = \Gamma_2$. The agreement between the two methods decreases with an increase Ω_{21}, with the master equation approach being more reliable. 14

1.8 Three Level Λ Scheme 16

1.9 $Im[\chi_{31}]$ for the three level Λ scheme with $\Omega_{21} = \Gamma_3/10$, $\Omega_{32} = \Gamma_3$ and $\gamma = \Gamma/100$. $Im[\chi_{31}]$ vanishes when $\Delta_{21} = \Delta_{32}$ resulting in an absorption coefficient of zero for the probe beam. The narrow peak at increased Δ_{32} is the result of simultaneous absorption of a probe and meter photon. 17

1.10 $Im[\chi_{21}]$ for the three level cascade scheme from Figure 1.6 with $\Omega_{21} = \Gamma_2/10$, $\Omega_{32} = \Gamma_2$ and $\Delta_{32} = \Gamma_{21}$. The dashed black line is $Im[\chi_{21}]$ for the Λ scheme with the same meter and probe beam powers and $\Delta_{32} = -\Gamma_2$. In the cascade scheme, because Γ_3 is generally not negligible, the dark state has a decay rate which, even in the ideal limit, reduces the induced transparency. This can be seen by the increase in $Im[\chi_{21}]$ at $\Delta_{21} = -\Delta_{32}$ as Γ_3 increases. . . . 18

2.1 (Right)Phase shift, L_{eff}, and $|\theta_0|$ at several two photon detunings, a $50nW$ probe beam and a $2\mu W$ meter beam. It can be seen from the plots that the ideal detuning of the meter beam is $\Delta_{32} = 0$, and because $\delta_+ = \Delta_{32} + \Delta_{21}$, the ideal two photon detuning is $\delta_+ = \Delta_{21}$. Decreasing δ_+ results in less overlap of the region of non-negligible L_{eff} and $|\theta_0|$. Increasing δ_+ instead of decreasing it produces the same curves mirrored on the X and Y axes. Calculations made for a $1cm$ long cloud of cold atoms with $OD = 100$. (Left) Three level cascade scheme used for cross phase modulation experiment. . 24

2.2 (Left) Maximum phase shift as a function of optical depth for warm atoms and cold atoms at several meter beam powers, for a $1nW$ probe beam, or equivalently a probe beam containing, on average, 4.29 photons ever nanosecond. The phase shift saturates around $OD = 20$ for cold atoms and $OD = 200$ for warm atoms. Curves are labeled with their single photon detuning.(Right) Phase shift, L_{eff} and θ_0 for cold and warm atoms with a $50nW$ probe beam and a $2\mu W$ meter beam. The curve for warm atoms has been plotted for the single photon detunings where the theory is valid, $\Delta_{21} >> 50MHz$. Calculations made for a $1cm$ cloud of atoms. The temperature of the cloud is $1mK$ for cold atoms, and $350K$ for warm atoms. Plots on the right are made for $OD = 100$. 26

2.3 Maximum phase shift as a function of probe beam power for several meter beam powers. The slope of this relationship corresponds to the phase shift imparted on the meter beam per probe photon. Each line is labeled with it's phase shift per photon in units of miliradians per photon, assuming the power corresponds to number of photons every $5ns$. Calculation done for a $1cm$ cloud of cold atoms with $OD = 100$. 27

2.4 The phase imparted on a meter beam over the course of time it takes a probe pulse with FWHM=1μs to propagate through the cold atom cloud for several probe powers. The dashed line is the phase shift for the hypothetical, non-physical case where the group velocity of the probe is not changed, and is plotted to show how the lowered group velocity of the probe effects the phase shift of the meter. Calculations made for a $1cm$ cloud of cold atoms at $OD = 100$. 28

2.5 Transmission of a meter beam at several powers modulated by a $1nW$ probe beam. Calculations done for a $1cm$ long cloud of cold atoms with $OD = 100$. 31

2.6 Transmission of a $600pW$ meter beam modulated by a $825pW$ probe beam for several single photon detunings, as a function of optical depth. Calculations done for a $1cm$ long cloud of cold atoms. 32

3.1 Optics scheme for EIT-based the dichroic atomic vapor laser lock. Two magnets (M) on either side of a cesium cell provide the magnetic field that breaks the degeneracy in the Zeeman levels. The component labeled DPD is a differential photo diode that's output is the difference of it's two input signals. *[Label Key:BG=Bragg Grating, BL=Beam launcher, BS=Beam Splitter, DPD=Differential photodiode, FI=Faraday Isolator, M=Magnet, PBS=Polarizing beam splitter, QWP=Quarter wave plate]* 34

3.2 (Left) Effect of Magnetic field breaking the degeneracy of Zeeman sub-levels and the level coupling provided by the polarized light. (Right) Absorption of light in the cesium cell as the frequency is swepped through resonance. In the presence of a magnetic field, the black curve is for linearly polarized light, and the red and blue curves are for σ^+ and σ^- light, respectively. The green curve is the error signal, acquired by subtracting the blue signal from the red. 35

3.3 (Right) Level scheme for the DAVLL+EIT locking technique. By sweeping Δ_{32}, the transparency window provided by EIT can be scanned through the detunings of σ^+ and σ^-. Measuring the transmission of each polarization provides two offset gaussian signals, like those used in the two level DAVLL scheme, that are used to acquire an error signal crossing zero at the locking frequency. (Left Top) Blue curve is the electrical error signal resulting from subtracting one polarization transmission signal from the other. Green curve is the signal from the $794nm$ laser diode controller that represents the scan in frequency. (Left Middle) Error signal with a reduced $794nm$ frequency scanning range. (Left Bottom) Error signal resulting from an increased magnetic field across the cesium cell. The detunings of the polarizations are moved farther apart, resulting in less overlap of the gaussian transmission signals that appears as the change in the slope of the error signal. 36

3.4 Beat note generated from locked ECDL laser and Titanium Sapphire laser tuned close to $794nm$. It appears the linewidth of the locked laser is on the order of megahertz. A noticeable difference was observed between the stability of the peak when the ECDL was locked, and when it was unlocked. 37

3.5 Optics setup for the main experimental apparatus. The experimental lasers and dipole trap are overlapped and coupled into the fiber from bellow with a mirror coated prism. The dipole trap is orthogonally polarized to the experimental lasers so that it can be removed with a polarizing beam splitter, while the experimental lasers will be separated with a Bragg grating. *[Label Key:BD=Beam dump, BG=Bragg Grating, BL=Beam launcher, BS=Beam Splitter, HWP=Half wave plate, PBS=Polarizing beam splitter]* 40

3.6 (Left) Image of MOT taken by observing the shadow the MOT casts when backlight with resonant laser light. (Right) Data collected for number of atoms re-trapped by dipole laser after a period of shutoff time. Used to calculate the temperature of atoms in the fiber. Picture and data produced by post-doctoral researcher Taehyun Yoon. 41

3.7 Design of the interferometer used to test the phase modulation measurement technique. One path contains a segment of HCPF that can be moved in and out of the beam, the other a retor-reflector on a translation stage to adjust the length of the path. Two $13mm$ focal length lenses (FL) were used to couple light into the fiber and then recollimate it after it exited the fiber. . 43

3.8 (Left) Photodiode signal as the frequency of the light in the interferometer is scanned. The frequency of oscillation obeys Eq. 3.2 and can be used to find Δd. In this fit, $\Delta d = 18.09cm$. (Right) Path length measurements for the interferometer when the HCPF was present and absent. There is a noticeable change between the two cases, but a large amount of noise is clearly present. 44

4.1 (A) Experimental setup for an optical Transistor. A cloud of cold atoms is trapped in a cavity and probed with three different lasers, a few photon gate beam, a strong control beam, and a source beam resonant with the cavity. (B) A gate pulse is stored in the atomic cloud by adiabatically reducing the control while the pulse is in the cloud, populating the $|s\rangle$ state. (C) The presence of atoms in the $|s\rangle$ state changes the resonance of the cavity, reflecting the once transmitted source beam. (D) The control is applied again, recovering the gate pulse and changing the cavity resonance back to normal. Figure acquired from *All-Optical Switch and Transistor Gated by One Stored Photon*[6] 47

B.1 (Left) Lens radius of curvature resulting from different settings of the beam splicer. (Right) Difference between the actual length of NCF spliced to a CF and the intended length. Two target lengths were used, $400\mu m$ and $370\mu m$. 55

B.2 (Top) Diagram of lens tipped fiber. A segment of core-less fiber (NCF) of length L is spliced onto a cored fiber (CF) and then melted to form a lens with radius R. The beam radius leaving the core is $\omega_1 = 2.75\mu m$ and has a minimum radius ω_2 after traveling a distance d from the fiber tip. (Bottom) Microscope image of the fabricated lens tipped fiber for which the focal length and beam waist was measured. 56

B.3 Calculation predictions for the focal point distance from fiber tip and the radius of the beam at the focal point for several radii of curvature as a function of NCF. 57

B.4 (Left) Microscope picture of razor blade used to measure focal distance and beam radius with the fiber. (Right) Measured beam radius with fit to Eq. B.7. The fit predicts a minimum beam radius of $4.5\mu m$, but the measured value is closer to $40\mu m$. 58

C.1 Circuit used to lock ECDL in DAVLL+EIT scheme. *Op-Amp: U1-U5=TL081. Resistors: R1=12KΩ, R2=10KΩ, R3=12KΩ, R4=100KΩ, R5=8.2KΩ, R6=8.2KΩ, R7=12KΩ, R8=8.2KΩ, R9=8.2KΩ, R10=1.5KΩ, R11=18KΩ, R12=18KΩ, R13=18KΩ, R14=18KΩ, R15=100KΩ, R16=12KΩ, R17=12KΩ, R12=18KΩ. Capacitors: C1=1μF, C2=100μF, C3=10nF* 62

C.2 Characterization of the circuit in figure C.1. (Left) Bode plot, showing a rapid dropoff in the output power as the frequency of the input signal is increased. (Right) Phase of the output signal as a function of the frequency of the input signal. 63

C.3 Locking circuit mounted in 3D printed lockbox, with the signal input, signal output and power input cables attached. Variable resistors are placed to allow access when the box is closed. 64

Chapter 1

Introduction

1.1 Motivation

Electromagnetic waves have a number of properties that make them appealing for applications in quantum computing schemes. They have many degrees of freedom, including wavelength, phase, polarization and field strength, that can be used to encode information. In addition, electromagnetic waves can traverse very large distances with minimal change in their characteristics. However, they do not interact with other electromagnetic waves by themselves, which presents a problem for quantum computing schemes that rely on light for information transfer and processing.

Several methods of quantum information processing have been proposed that would be achievable if significant interactions between beams of light were possible. The Kerr effect, in which an applied electric field changes the index of refraction of a material, is utilized in a number of these schemes. One proposed method involves using this effect to construct single photon sources and detectors and two qubit parity gates, and then using these elements in two possible quantum computing schemes [19]. Another method would be to achieve qubit-qubit interactions by connecting qubits with an optical information bus, the bus interacting with the qubits through the Kerr effect [22]. This would allow qubits to be spaced apart from each other and avoid unwanted nearest neighbor interactions and allow individual qubits to be probed without effecting others. For these schemes to be feasible, a few photon signal beam must be able to change the index of refraction of a medium by enough to cause a phase shift in a stronger beam by 1×10^{-5} to 1×10^{-2} radians per weak beam photons.

It is also possible to achieve interactions between electromagnetic waves through the simultaneous absorption of two photons by a medium. This can be used for all optical switching, where the presence of one laser can control the transmission of another [31][14]. It has also been shown that the quantum Zeno effect can be used to implement quantum logic gates, with the Zeno effect brought about through the use of two-photon absorption [10]. By coupling a system to a two-photon absorbing atomic medium, measuring the excited state of the atoms is identical to measuring the first system. These quantum Zeno gates can also be used with other two-photon absorbing systems to create heralded single-photon sources [13].

The largest obstacle to implementing these effective photon-photon interactions is that the effects of the few photon fields necessary for quantum computing can be small and difficult to measure, and attenuation of light fields by absorption is usually high for frequencies of light that interact strongly with matter. Sophisticated fabrication technology and using low temperature atoms to take advantage of coherent effects reduces the impact of these issues.

One technique that has been successfully used to amplify the effects of low powered light is to confine atoms and fields to a very small volume, ensuring that atoms are localized in the vicinity of the field. Advances in fabrication techniques over the past decades have made photonic crystals appealing candidates to provide this confinement. Figure 1.1 shows several examples of photonic crystals that can guide light into a region populated with atoms. The specific photonic crystal type used for the work described in this thesis are called hollow core photonic crystal fibers (HCPF) [8]. The hollow, waveguide section of these fibers can be loaded with cold atoms to create the tight confinement of light and matter described above.

Further amplification of nonlinear optical effects can be achieved by taking advantage of quantum coherence effects that are present close to atomic resonance. Electromagnetically induced transparency is one such effect where the absorption pathways of two light fields add destructively, greatly reducing the absorption of light near and at atomic resonance. The phenomena of slow light, in which a gradient in the refractive index of a material with respect to an indecent field's frequency causes a reduction in group velocity, is another coherent effect that can be utilized. Increasing the time an electric field remains in the vicinity of atoms increases the chance of interactions involving multiple photons. Both of these effects require low decoherence rates and groups of atoms that have nearly identical interactions with an electric field. This is much more difficult to achieve with room temperature atoms in HCPF than with cold atoms, as warm atoms have large decoherence rates due to movement through an inhomogeneous optical field, and collisions with the walls of the fiber [21].

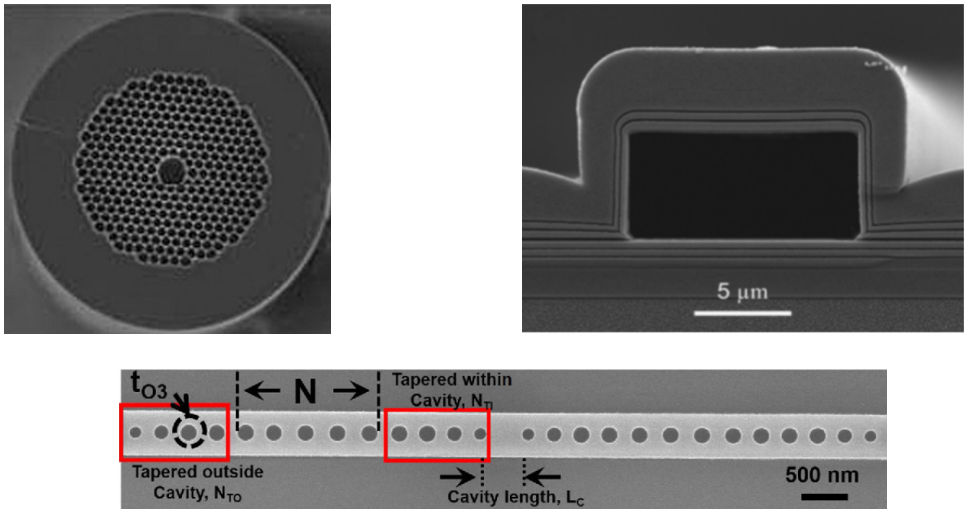

Figure 1.1: (Top Left) Hollow Core Photonic Crystal Fiber, Thorlabs product HC-1550. (Top Right) Hollow core ARROW waveguide [17]. (Bottom) One dimensional photonic crystal wire [20]

In this thesis, two techniques for effective photon-photon interactions at low light levels will be explored. The first method is the modification of the phase of one beam of light with another, much weaker beam. In the second method, the transmission of a beam of light through a cloud of cold atoms will be controlled by using a second beam to induce two photon absorption. It will be shown that the effectiveness of these techniques is improved by using cold atoms capable of exhibiting coherent effects, and the consequences of these effects will be explored. In addition to this, work on the experimental preparation necessary to perform these experiments will be discussed.

1.2 Two Level Atom

Consider a two level atom placed in an electric field $\vec{E}$ with frequency ω that couples the atom's ground state $|1\rangle$ to its excited state $|2\rangle$, as shown in Figure 1.2. The energy difference between $|1\rangle$ and $|2\rangle$ is $\hbar\omega_{21}$ and the electric field's detuning from atomic resonance is $\Delta = \omega - \omega_{21}$. If the atom is initially in the ground sate, it can absorb a photon from the field and transition to the excited state. From the excited state $|2\rangle$, the atom will eventually emit a photon and transition back to $|1\rangle$, either by stimulated emission, or by spontaneous emission into another mode of the electric field. The latter happens at a rate

of $\Gamma/2$, where Γ is the linewidth of the atomic transition. This system is described by the wave-function $|\psi\rangle = c_1 |1\rangle + c_2 |2\rangle$, where the state coefficients c_1 and c_2 are functions of time and the probability of finding the atom in state $|1\rangle$ or $|2\rangle$ is $|c_1|^2$ and $|c_2|^2$ respectively.

There are several analytic methods that can be used to study the atom's response to the electric field. Here, the density matrices' master equation will be solved under a few simple approximations [25], while in a future section, a stochastic wave-function approach will be employed for the more complex three level case. The Hamiltonian for a two level atom in the electric field described above, and interacting with the field within the dipole approximation, is

$$H = \hbar\omega_{21}\sigma^\dagger\sigma - \vec{E}\cdot\vec{d} \tag{1.1}$$

where $\sigma = |1\rangle\langle 2|$ and $\vec{d}$ is the dipole operator which can be expressed in terms of σ as $\vec{d} = \vec{\mu_{21}}(\sigma + \sigma^\dagger)$ where $\vec{\mu_{21}}$ is the transition dipole moment between $|1\rangle$ and $|2\rangle$. Consistent with the dipole approximation, the spatial dependence of the electric field will be ignored, as the wavelength of the light is assumed to be much larger than the size of the atom so the atom experiences a constant electric field strength across its length. The electric field can then be written as $\vec{E} = \hat{\epsilon}\mathcal{E}_0(e^{-i\omega t} + e^{i\omega t})$, and substituting this into the interaction term in the Hamiltonian gives

$$H_{int} = -\vec{E}\cdot\vec{d} = -\mu_{21}\mathcal{E}_0(e^{-i\omega t}\sigma + e^{-i\omega t}\sigma^\dagger + e^{i\omega t}\sigma + e^{i\omega t}\sigma^\dagger). \tag{1.2}$$

Looking at the time evolution of the free atomic Hamiltonian reveals that the expectation value of σ carries a $e^{-i\omega_{21}t}$ time dependence. Terms in the expectation value of H_{int} will then have oscillating time dependence with frequencies $|\omega_{21} - \omega|$ or $|\omega_{21} + \omega|$. For optical frequencies, where ω is on the order of 10^{14}, and when ω_{21} is close to resonance, $|\omega_{21} + \omega|$ is extremely large and contributions from terms oscillating at this frequency average to zero on time scales larger than femtoseconds. It is a valid and well known approximation to drop these rapidly oscillating terms from Eq. 1.2, and is known as the rotating-wave approximation (RWA). Interestingly, the RWA approximation is valid whenever another approximation that was implicitly assumed earlier is valid [25]: that the electric field is tuned close enough to resonance with $|2\rangle$ that excitations to any other excited state can be ignored.

Another way to eliminate explicitly time dependent terms in Eq. 1.1 is to perform a rotating frame transformation. The Hamiltonian in the rotating frame is denoted $\tilde{H}$ and is defined to be

$$\tilde{H} = UHU^\dagger + i\hbar(\partial_t U)U^\dagger \tag{1.3}$$

where U, for the two level case, is the unitary transformation

$$U = Exp[i\omega t\,|2\rangle\langle 2|] \tag{1.4}$$

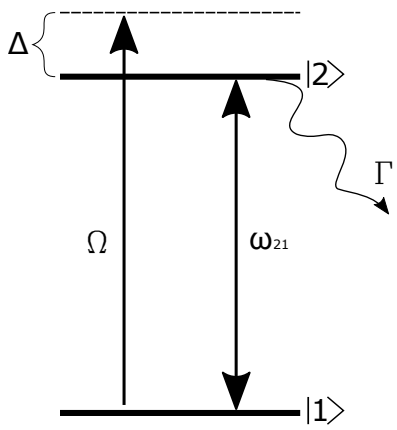

Figure 1.2: Two level atom interacting with an electric field. The energy separation of the levels is $\hbar\omega_{21}$

that takes the state vector in the lab frame $|\psi\rangle$, to the rotating frame $|\tilde{\psi}\rangle$, as

$$U|\psi\rangle = |\tilde{\psi}\rangle = \tilde{c_1}|1\rangle + \tilde{c_2}|2\rangle \tag{1.5}$$

where $\tilde{c_1} = c_1$ and $\tilde{c_2} = e^{i\omega t}c_2$. Combining the RWA with this frame transformation produces the Hamiltonian

$$\tilde{H} = -i\hbar\Delta\sigma^\dagger\sigma - \hbar\Omega(\sigma + \sigma^\dagger) \tag{1.6}$$

with the Rabi frequency $\Omega = \frac{\mu_{21}\mathcal{E}_0}{\hbar}$ and field detuning from resonance Ω.

The equations of motion for the atom can now be found by solving the master equation of the density matrix $\tilde{\rho} = |\tilde{\psi}\rangle\langle\tilde{\psi}|$,

$$\partial_t\tilde{\rho} = -\frac{i}{\hbar}[\tilde{H}, \tilde{\rho}] + \Gamma\mathcal{D}[\sigma]\tilde{\rho} \tag{1.7}$$

where $\mathcal{D}$ is the Lindblad superoperator

$$\mathcal{D}[c]\rho = c\rho c^\dagger - \frac{1}{2}(c^\dagger c\rho + \rho c^\dagger c). \tag{1.8}$$

This produces a set of coupled differential equations for the matrix elements of $\tilde{\rho}$,

$$\begin{aligned}
\partial_t\tilde{\rho}_{11} &= i\Omega(\tilde{\rho}_{21} - \tilde{\rho}_{12}) + \Gamma\tilde{\rho}_{22} \\
\partial_t\tilde{\rho}_{22} &= i\Omega(\tilde{\rho}_{12} - \tilde{\rho}_{21}) - \Gamma\tilde{\rho}_{22} \\
\partial_t\tilde{\rho}_{12} &= i\Omega(\tilde{\rho}_{22} - \tilde{\rho}_{11}) - (\frac{\Gamma}{2} + i\Delta)\tilde{\rho}_{12} \\
\partial_t\tilde{\rho}_{12} &= i\Omega(\tilde{\rho}_{11} - \tilde{\rho}_{22}) - (\frac{\Gamma}{2} - i\Delta)\tilde{\rho}_{21},
\end{aligned} \tag{1.9}$$

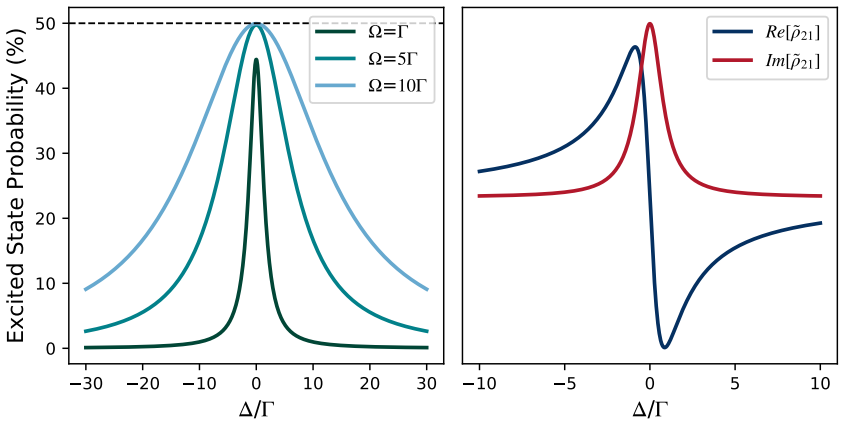

Figure 1.3: (Left) Probability of finding a two level atom in the excited state as a function of Δ/Γ for increasing Rabi frequencies, found from $\tilde{\rho}_{22}$ in Eq. 1.10 . It can be seen that the probability saturates at 50%, and further increases in Rabi frequency broaden the peak. (Right) Real and imaginary parts of $\tilde{\rho}_{21}$ from Eq. 1.10 for $\Omega = \Gamma/2$. As will be discussed in section 1.3, the real part determines the index of refraction of the atom as experienced by the field, and the imaginary part is proportional to the absorption coefficient of the atom.

where the state coefficients have been replaced with matrix elements of $\tilde{\rho}$ using the relation $\tilde{\rho}_{ij} = c_i c_j^\dagger$. Because the atom has a decoherence rate, there exists a steady state solution to these equations where $\partial_t \tilde{\rho} \to 0$ as $t \to \infty$. Setting $\partial_t \tilde{\rho} = 0$, Eq. 1.9 can be solved algebraically with the additional equations $\tilde{\rho}_{11} + \tilde{\rho}_{22} = 1$ and $\tilde{\rho}_{12} = \tilde{\rho}_{12}^\dagger$. Doing so produces the equations

$$\begin{aligned} \tilde{\rho}_{22}(t \to \infty) &= \frac{\Omega^2}{\Delta^2 + \frac{\Gamma^2}{4} + 2\Omega^2} \\ \tilde{\rho}_{21}(t \to \infty) &= \frac{-\Omega(\Delta - i\frac{\Gamma}{2})}{\Delta^2 + \frac{\Gamma^2}{4} + 2\Omega^2}, \end{aligned} \tag{1.10}$$

which are plotted in Figure 1.3. For ease of notation, the tilde indicating that a parameter is in the rotating frame will be omitted for the remainder of this thesis, and atomic equations of motion will be assumed to be in the rotating frame.

1.3 Atomic Media

So far this discussion has dealt with the effect an electric field has on one atom, but no mention has been made as to how the atom's induced electric dipole moment effects the overall electric field. In fact, a single atom would not have an observable effect, but the combined dipole moments of a group of atoms could. In order to study the properties of an electric field propagating through a media consisting of an ensemble of atoms, a quantity that describes the collective dipole moment of the ensemble is required. This macroscopic quantity is the polarization of the media, and is defined

$$\vec{P_{ij}} = N(\vec{\mu}_{ij}\rho_{ij} + \vec{\mu}^*_{ij}\rho_{ji}) \tag{1.11}$$

for a medium with atomic density N and electric field $\vec{E}$ coupling states $|i\rangle$ and $|j\rangle$. Analytically, the polarization appears as a source term in Maxwell's equations,

$$\begin{aligned} \boldsymbol{\nabla} \times \vec{E} &= -\frac{\partial \vec{B}}{\partial t} \\ \boldsymbol{\nabla} \times \vec{B} &= \frac{1}{c^2}\frac{\partial}{\partial t}(\vec{E} + \frac{1}{\epsilon_0}\vec{P}) \end{aligned} \tag{1.12}$$

where c is the speed of light and ϵ_0 is the permittivity of free space. These two equations can be combined to give the wave equation for $\vec{E}$,

$$\boldsymbol{\nabla}^2\vec{E} - \frac{1}{c^2}\frac{\partial^2\vec{E}}{\partial t^2} = \frac{1}{\epsilon_0 c^2}\frac{\partial^2\vec{P}}{\partial t^2} \tag{1.13}$$

Under the assumption that the electric field is nearly monochromatic, it and the polarization can be written as

$$\begin{aligned} \vec{E}(r,t) &= \vec{\mathcal{E}}(r,t)e^{ik(z-ct)} + c.c. \\ \vec{P}(r,t) &= \vec{\mathcal{P}}(r,t)e^{ik(z-ct)} + c.c. \end{aligned} \tag{1.14}$$

with envelopes $\vec{\mathcal{E}}$ and $\vec{\mathcal{P}}$ and wavenumber k.

Often, it is useful to consider the case where the frequency ω, called the carrier frequency, oscillates on a much faster time scale than the features of the envelopes. Taking this into account is a common technique known as the slowly-varying envelope approximation

(SVEA), and can be expressed through the inequalities

$$\begin{aligned} |\omega\vec{\mathcal{P}}| &>> |\frac{\partial}{\partial t}\vec{\mathcal{P}}| \\ |\omega\vec{\mathcal{E}}| &>> |\frac{\partial}{\partial t}\vec{\mathcal{E}}| \\ |k\vec{\mathcal{E}}| &>> |\frac{\partial}{\partial z}\vec{\mathcal{E}}|. \end{aligned} \tag{1.15}$$

This approximation is applied by substituting Eq. 1.14 into Eq. 1.13 and then dropping terms according to Eq. 1.15 and gives, for a planewave propagating in the z direction,

$$\frac{\partial}{\partial z}\mathcal{E} + \frac{1}{c}\frac{\partial}{\partial t}\mathcal{E} = \frac{ik}{2\epsilon_0}\mathcal{P}. \tag{1.16}$$

For a linear dielectric medium, the polarization is related to the electric field by

$$\mathcal{P} = \epsilon_0\chi\mathcal{E}, \tag{1.17}$$

where the proportionality constant χ is called the susceptibility of the medium and can be found by combining Eq. 1.11 with Eq. 1.18 to produce

$$\chi_{ij} = \frac{N\mu}{\epsilon_0\mathcal{E}}\rho_{ij} \tag{1.18}$$

Eq. 1.16 can now be trivially solved by moving to the Fourier domain where its solution is

$$\mathcal{E}(\partial\omega, z) = \mathcal{E}(\partial\omega, 0)e^{iz(\partial\omega/c + ik\chi(\partial\omega))/2}, \tag{1.19}$$

and then by transforming back into the time domain [16]

$$\mathcal{E}(t, z) = \int d(\partial\omega)e^{-i\partial\omega z}\mathcal{E}(\partial\omega, 0)e^{iz(\partial\omega/c + ik\chi(\partial\omega))/2}. \tag{1.20}$$

To understand the physical effects of the susceptibility, and thus the effect the atoms in the media have on the electric field, it is informative to look at Eq. 1.20 in the case of a few simplifying assumptions. First, if the electric field is entirely monochromatic, its Fourier transom is the delta function $\mathcal{E}(\partial\omega) = \mathcal{E}_0\delta(\partial\omega)$ and the solution to Eq. 1.20 is simply

$$\mathcal{E}(t, z) = \mathcal{E}_0 e^{ik\chi(0)z/2}. \tag{1.21}$$

For small χ, which is the case for the weak field limit in the SVEA regime, the real part of the susceptibility can be understood as a modification of the index of refraction, which

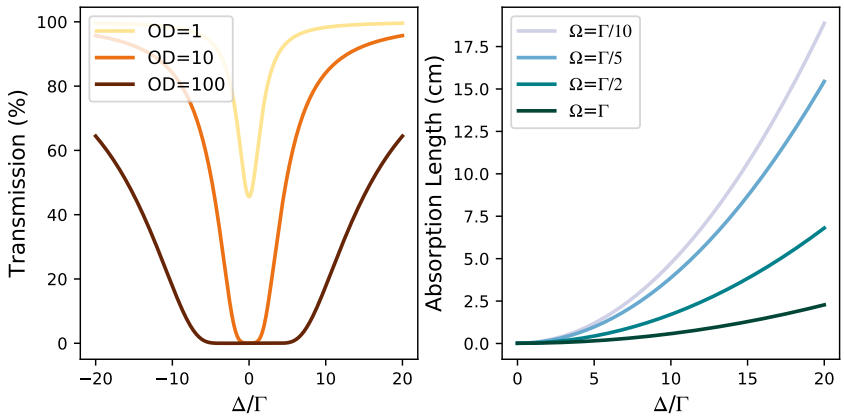

Figure 1.4: (Left) Transmission of light through a one centimeter length cloud of two level atoms for several optical depths and $\Omega = \Gamma$. (Right) Absorption length for an atomic cloud with optical depth of one hundred and varied Rabi frequencies.

can be written in terms of the susceptibility as $n = \sqrt{1+\chi}$. This indicates that for small χ,

$$n = 1 + \frac{Re[\chi]}{2} \tag{1.22}$$

and thus the real part of susceptibility determines the light's phase velocity $v_p = c/n$. The imaginary part of the susceptibility introduces to the field a real, exponentially decaying coefficient $Exp[-\alpha z/2]$, where α is called the absorption coefficient and is defined

$$\alpha = kIm[\chi]. \tag{1.23}$$

The value of α determines the rate at which the light's intensity decreases as it travels a distance z. The absorption length is the distance light must travel so that the ratio of initial intensity to final intensity is $1/e$ and is equal to $1/\alpha$. The absorption length for several Rabi frequencies is shown in Figure 1.4

The next simplest case to consider is nearly monochromatic light, such as a plane wave with a broad Gaussian envelope,

$$\mathcal{E}_g(t,z) = \mathcal{E}_0 Exp[-\frac{4ln2}{L_t^2}(t - z/c)^2] \tag{1.24}$$

where L_t is the full width at half max of the pulse in time. In this case, frequency dependence of the susceptibility can be removed by taking the Taylor series expansion around

the carrier frequency,

$$\chi(\partial\omega) = \chi(0) + \omega\frac{\partial\chi}{\partial\omega}\bigg|_{\omega=0} + \mathcal{O}(\partial\omega^2). \tag{1.25}$$

Dropping second order terms, substituting this into Eq. 1.20 and performing the integration gives

$$\mathcal{E}(t,z) = e^{izk\chi(0)/2}\mathcal{E}_g(t - z/v_g, 0) \tag{1.26}$$

where v_g is the group velocity, which can be expressed in terms of the susceptibility as

$$v_g = \frac{c}{1 + \frac{\omega}{2}\frac{\partial\chi}{\partial\omega}}. \tag{1.27}$$

An important aspect of Eq. 1.27 is that the derivative of the susceptibility in the denominator is multiplied by the carrier frequency of the light, which is on the order of 10^{14} for optical frequencies. This means that even a small dependence of susceptibility on frequency can lead to a large reduction in the group velocity, and produce the phenomenon known as slow light.

Having established the absorptive properties of an atomic medium, it is convenient to define a measure of its opacity called the optical depth (OD), which is dimensionless and defined as

$$OD = N\sigma_0 L, \tag{1.28}$$

for resonant scattering cross section σ_0, and length of medium L. To calculate the optical depth of a system, σ_0 must be found, and this is done in the following way. The scattering cross section σ_{sc} is related to the scattered power P_{sc} by

$$P_{sc} = \sigma_{sc} I_{in}, \tag{1.29}$$

where I_{in} is the incident field intensity, which for a field of Rabi frequency Ω is

$$I_{in} = \frac{1}{2}c\epsilon_0|\frac{\hbar\Omega}{\mu}|^2. \tag{1.30}$$

The scattered power can also be given as

$$P_{sc} = \hbar\omega\Gamma\rho_{22} \tag{1.31}$$

because this is the energy of a photon multiplied with the rate the photons are emitted. The scattering cross section can then be expressed as

$$\sigma_{sc}(\Delta) = \frac{\hbar\omega\Gamma}{I_{in}}\rho_{22}(\Delta) \tag{1.32}$$

and the resonant scattering cross section is simply $\sigma_0 = \sigma_{sc}(0)$. Figure 1.4 shows the transmission of light through a one centimeter long cloud of atoms for different optical depths.

The optical depth is a useful quantity when comparing the optical properties of media with different temperatures. As will be seen in the next section, ρ_{22} is temperature dependent and therefore σ_0 is as well, meaning clouds of atoms with identical atomic density but different temperature will have different optical depths. When making comparisons at different temperatures, common optical depths will be chosen and Eq. 1.28 will be used to find the corresponding atomic densities.

1.4 Atomic Motion

The equations in Section 1.2 were found under the implicit assumption that the atom was stationary with respect to an electromagnetic field during their interaction. When making predictions about physical systems, it will be necessary to consider the effects of atomic motion. This effect is present because atoms moving parallel to the propagation direction of the electromagnetic field will experience a shifted frequency described by the Doppler effect. An atom moving at a velocity v parallel with respect to an electromagnetic field of frequency ω will see a frequency ω_d defined

$$\omega_d = \omega(1 + v/c) \tag{1.33}$$

where c is the speed of light.

An ensemble of atoms contains a distribution of velocities that depends on its temperature. The Maxwell-Boltzmann distribution gives the fraction of atoms with velocities between v and $v + dv$ for one dimensional motion as $P(v)dv$ defined

$$P(v)dv = \sqrt{\frac{m}{2\pi kT}} e^{\frac{mv^2}{2kT}} dv \tag{1.34}$$

where m is the mass of an atom, k is Boltzmann's constant, and T is the temperature of the ensemble. Now to find the susceptibility, it is necessary to consider contributions from atoms of different velocities. This is done by integrating the susceptibility at a given frequency over all velocities, weighted by the Maxwell-Boltzmann distribution, and gives the Doppler broadened susceptibility χ_d as

$$\chi_d(\omega) = \int_{-\infty}^{\infty} P(v)\chi(w[1 + v/c])dv \tag{1.35}$$

The real and imaginary parts of χ_d, for a two level atom, are plotted in Figure 1.5 for several temperatures and show that the effects of atomic motion mostly appear close to resonance, where narrow features of the susceptibility are broadened and shortened, while off resonant behavior remains fairly unchanged.

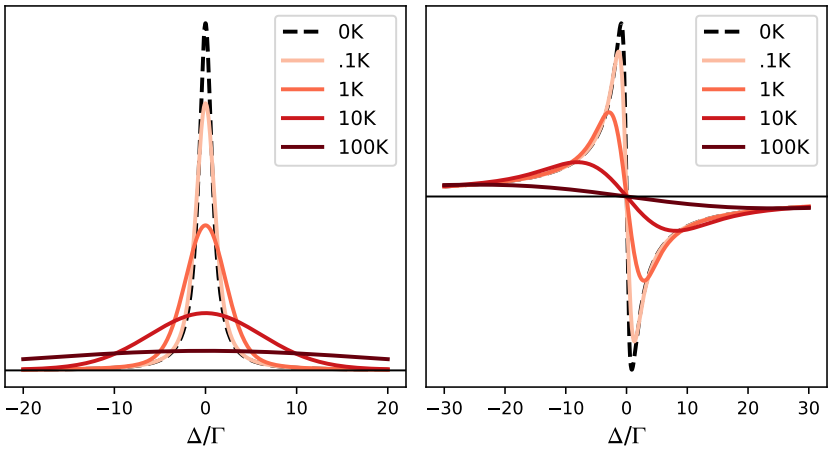

Figure 1.5: Imaginary (left) and real (right) parts of the susceptibility of an ensemble of two level atoms at several temperatures. Higher temperatures reduce and broaden features near resonance, though off resonant behavior remains nearly the same. Horizontal black lines mark zero

1.5 Three Level Atom of Ladder Type

Adding a third energy level to the previous scheme with an accompanying electric field, as shown in Figure 1.6, produces a system with much richer physics than the two level case. Quantitative analysis of this system begins with two steps that were previously employed to eliminate explicit time dependence from the two level Hamiltonian, taking the rotating wave approximation and making a rotating frame transformation,

$$H = -\hbar\Delta_{21}\sigma_1^\dagger\sigma_1 - \hbar\delta_+\sigma_2^\dagger\sigma_2 - \hbar\Omega_{21}(\sigma_1 + \sigma_1^\dagger) - \hbar\Omega_{32}(\sigma_2 + \sigma_2^\dagger). \tag{1.36}$$

where $\Delta_{21} = \omega_p - \omega_{21}$ and $\Delta_{32} = \omega_m - \omega_{32}$ are the single photon detunings and $\delta_+ = \Delta_{21} + \Delta_{32}$ is the two photon detuning, σ_1 and σ_2 denote the matrices $|1\rangle\langle 2|$ and $|2\rangle\langle 3|$ respectively, and Ω_{21} and Ω_{32} are the Rabi frequencies of the driving fields. The frequencies of the driving fields are ω_p and ω_m for the $|1\rangle \to |2\rangle$ and $|2\rangle \to |3\rangle$ transitions respectively.

From here it would be possible to solve the master equation for the density matrix, as was done for the two level case, but the solution would take a very complicated form. It is simpler to take a different approach with one more approximation, that Ω_{21} is small enough that there is a very low probability of exciting the atom. This is called the weak field limit, and the quantitative statement of this approximation is $c_1 \approx 1$ and $\dot{c}_1 \approx 0$.

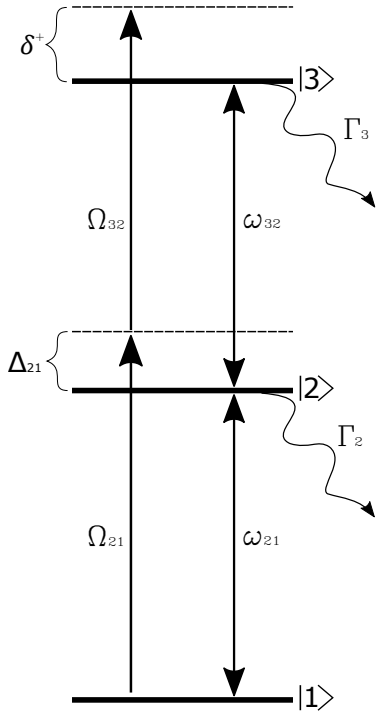

Figure 1.6: Three level Cascade scheme

Instead of solving the master equation, the state coefficients of the wavefucntion can be found from a non-hermitian, effective Hamiltonian H_{eff}, defined

$$\begin{aligned} H_{eff} &= H + H_\Gamma \\ H_\Gamma &= -i\hbar\frac{\Gamma_b}{2}\sigma_1^\dagger\sigma_1 - i\hbar\frac{\Gamma_c}{2}\sigma_2^\dagger\sigma_2 \end{aligned} \tag{1.37}$$

where Γ_2 and Γ_3 are the decay rates of state $|1\rangle$ and $|2\rangle$ respectively. By substituting this into the Schrödinger equation and taking the inner product with respect to $\langle 1|$ and $\langle 2|$ the equations of motion for the state coefficient can be obtained [25],

$$\begin{aligned} \dot{c}_2 &= (i\Delta_{21} - \frac{\Gamma_2}{2})c_3 + i\Omega_{32}c_3 + i\Omega_{21} \\ \dot{c}_3 &= (i\delta^+ - \frac{\Gamma_3}{2})c_3 + i\Omega_{32}c_2. \end{aligned} \tag{1.38}$$

As in the two level case, the presence of decoherence means there exists a steady state which the system approaches after a period of time. This state can be found by setting $\dot{c}_2 = 0$ and $\dot{c}_3 = 0$ and solving the above coupled equations for c_2 and c_3. The resulting steady state equations are

$$\begin{aligned} c_2 &= \frac{-\Omega_{21}(\delta_+ + i\frac{\Gamma_3}{2})}{(\Delta_{21} + i\frac{\Gamma_2}{2})(\delta_+ + i\frac{\Gamma_3}{2}) - \Omega_{32}^2} \\ c_3 &= \frac{\Omega_{21}\Omega_{32}}{(\Delta_{21} + i\frac{\Gamma_2}{2})(\delta_+ + i\frac{\Gamma_3}{2}) - \Omega_{32}^2}. \end{aligned} \tag{1.39}$$

These are convenient analytic expressions that can be used to approximate the system's density matrix elements in the weak field limit, since

$\rho_{ij} \approx c_i c_j^\dagger$. This gives ρ_{32} as

$$\rho_{32} = \frac{-\Omega_{32}\Omega_{21}^2(\delta_+ - i\Gamma_3/2)}{(\Delta_{21}^2 + \Gamma_2^2/4)(\delta_+^2 + \Gamma_3^2/4) + \Omega_{32}^4 - 2\Omega_{32}^2(\Delta_{21}\delta_+ + \Gamma_2\Gamma_3/4)} \tag{1.40}$$

Figure 1.7 shows the matrix element $c_2 c_2^\dagger \approx \rho_{22}$, the population of state $|c_2\rangle$, plotted with the numerical solutions of the master equation at increasing Rabi frequencies, or equivalently increasing electric field powers. The numerical solutions are more accurate, but for low Ω_{21} and detunings away from resonance the agreement between the methods is good.

Figure 1.7 shows two peaks in the first excited state population, neither of which occur at $\Delta_{21} = 0$ as would be the case for a two level atom. The reason for this is a phenomenon called the AC Stark shift, in which an oscillating electric field, in this case represented with Ω_{32}, splits an atomic resonance into two resonances that are shifted in opposite directions by a function of Ω_{32}.

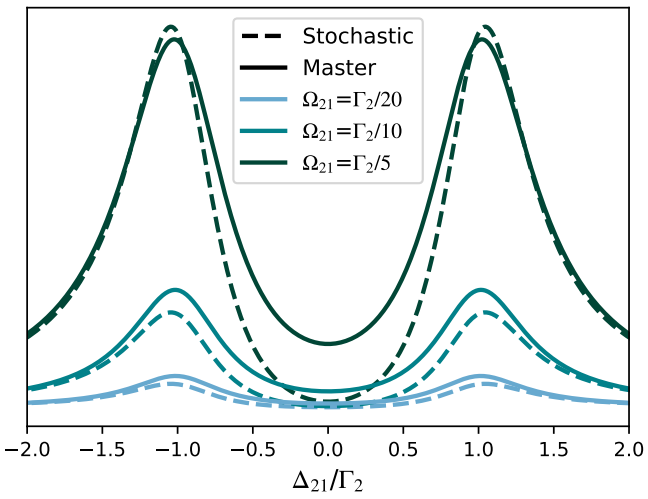

Figure 1.7: Comparison of density matrix element ρ_{22} calculated by numerically solving the master equation (solid line) and the stochastic wavefunction approach in the weak probe field limit (dashed line), for $\Delta_{32} = 0$ and $\Omega_{32} = \Gamma_2$. The agreement between the two methods decreases with an increase Ω_{21}, with the master equation approach being more reliable.

The AC Stark shift can be seen analytically by diagonalizing the interaction Hamiltonian and finding the eigenvalues of its dressed states. This will be done here for a limiting

case that will appear again in an illuminating context. The characteristic equation for the eigenvalues of the interaction Hamiltonian is

$$\lambda^3 + \hbar\lambda^2(\Delta_{21} + \delta_+) - \hbar^2\lambda(-\Delta_{21}\delta_+ + \Omega_{21}^2 + \Omega_{32}^2) - \hbar^3\delta_+\Omega_{32}^2 = 0. \tag{1.41}$$

In the case that $\delta_+ = 0$, the three eigenvalues are be found to be

$$\begin{aligned} \lambda_0 &= 0 \\ \lambda_+ &= -\frac{\hbar\Delta_{21}}{2} + \frac{\hbar}{2}\sqrt{\Delta_{21}^2 + 4\Omega_{21}^2 + 4\Omega_{32}^2} \\ \lambda_- &= -\frac{\hbar\Delta_{21}}{2} - \frac{\hbar}{2}\sqrt{\Delta_{21}^2 + 4\Omega_{21}^2 + 4\Omega_{32}^2}. \end{aligned} \tag{1.42}$$

It is clear that one dressed state always has zero energy while the other two are separated in energy by $\sqrt{\Delta_{21}^2 + 4\Omega_{21}^2 + 4\Omega_{32}^2}$. The split levels demonstrate the AC Stark shift, but the zero energy level plays a crucial role in electromagnetically induced transparency and it will be useful to find that its corresponding eigenstate in the bare state basis is $|\lambda_0\rangle = \frac{\Omega_{32}|1\rangle - \Omega_{21}|3\rangle}{\sqrt{\Omega_{21}^2+\Omega_{32}^2}}$.

1.6 Three Level Atom of Λ Type and Electromagnetically Induced Transparency

The ability to slow the group velocity of light has interesting applications in nonlinear optics, as will be discussed in the next section. Before that, it is useful establish a situation where a light pulse will be slowed with minimal absorption. This is complicated because regions of the susceptibility where the real part varies quickly with frequency are generally close to a resonance, where absorption is high. A solution to this is to take advantage of a phenomenon called electromagnetically induced transparency (EIT). EIT is usually studied in the Λ level scheme shown in Figure 1.8, and is characterized by high levels of transmission of nearly resonant light due to the action of another, stronger electric field. These two fields will be called the probe and control field respectively. The probe couples an initially populated hyperfine level of an atom's ground state, $|1\rangle$, with an excited level, $|3\rangle$, that is in turn coupled through the control to an unpopulated hyperfine level of the ground state, $|2\rangle$. The effective, non-Hermitian Hamiltonian for this interaction is H_λ and is given by

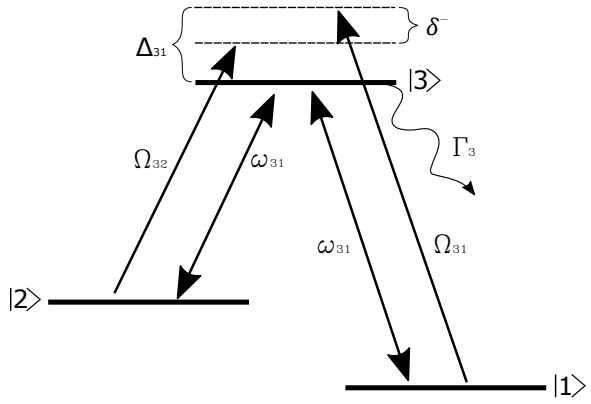

Figure 1.8: Three Level Λ Scheme

$$\begin{aligned} H_{atom} &= -\hbar\Delta_{31}\left|3\right\rangle\!\left\langle 3\right| - \hbar\delta_{-}\left|2\right\rangle\!\left\langle 2\right| \\ H_{int} &= -\hbar\Omega_{31}(\left|1\right\rangle\!\left\langle 3\right| + \left|3\right\rangle\!\left\langle 1\right|) - \hbar\Omega_{32}(\left|2\right\rangle\!\left\langle 3\right| + \left|3\right\rangle\!\left\langle 2\right|) \\ H_{\Gamma} &= -i\hbar\gamma\left|2\right\rangle\!\left\langle 2\right| - i\hbar\frac{\Gamma_3}{2}\left|3\right\rangle\!\left\langle 3\right| \\ H_{\lambda} &= H_{atom} + H_{int} + H_{\Gamma}. \end{aligned} \tag{1.43}$$

Here the two photon detuning is defined $\delta_{-} = \Delta_{31} - \Delta_{32}$, and Γ_3 is the decay rate of $|3\rangle$. It is reasonable in many cases to ignore the spontaneous decay of state $|2\rangle$, as transitions between hyperfine ground states are dipole forbidden and usually have lifetimes much larger than any of the time scales of the interaction, but there is a decoherence of the ground state γ, arising from atomic collisions. This can be taken to be small for slow moving cold atoms.

A quick way see how transparency can occur is to study the systems dressed states when both the probe and control fields are resonant, so that $\Delta_{31} = \Delta_{32} = 0$. In this case, in the ideal limit of $\gamma = 0$, the effective Hamiltonian is

$$\begin{aligned} H_{eff} &= -i\hbar\frac{\Gamma_3}{\hbar}\left|3\right\rangle\!\left\langle 3\right| - \hbar\Omega_{31}(\left|1\right\rangle\!\left\langle 3\right| + \left|3\right\rangle\!\left\langle 1\right|) - \hbar\Omega_{32}(\left|2\right\rangle\!\left\langle 3\right| + \left|3\right\rangle\!\left\langle 2\right|) \\ &= -i\hbar\frac{\Gamma_3}{\hbar}\left|3\right\rangle\!\left\langle 3\right| - \hbar(\Omega_{31}\left|1\right\rangle + \Omega_{32}\left|2\right\rangle)\left\langle 3\right| - \hbar\left|3\right\rangle(\Omega_{31}\left\langle 1\right| + \Omega_{32}\left\langle 2\right|). \end{aligned} \tag{1.44}$$

The second equation was written to show that $|3\rangle$ only couples to a particular superposition

of $|1\rangle$ and $|2\rangle$. This state is called the bright state $|B\rangle$ [25], and can be written

$$|B\rangle = \frac{\Omega_{31}|1\rangle + \Omega_{32}|2\rangle}{\sqrt{\Omega_{31}^2 + \Omega_{32}^2}}. \tag{1.45}$$

Another, orthogonal state exists, called the dark state because it does not fluoresce,

$$|D\rangle = \frac{\Omega_{32}|1\rangle - \Omega_{31}|2\rangle}{\sqrt{\Omega_{31}^2 + \Omega_{32}^2}}, \tag{1.46}$$

which is completely decoupled from the excited state, either through decay channels or field coupling. Transparency arises because atoms will accumulate in $|D\rangle$, since it does not decay and does not interact with the fields.

To show this analytically, the method used in Section 1.5 was employed. In the weak field limit with $c_1 \approx 1$ and $\dot{c}_1 \approx 0$, and for the steady state where $\dot{c}_2 \approx 0$ and $\dot{c}_3 \approx 0$, the state coefficients c_2 and c_3 can be found and used to derive the density matrix element ρ_{31} as

$$\rho_{31} = -\frac{i\Omega_{31}(\delta_- + i\gamma)}{(i\Delta_{31} - \frac{\Gamma_3}{2})(\delta_- + i\gamma) - i\Omega_{32}^2}. \tag{1.47}$$

As predicted, this term vanishes for $\Delta_{31} = \Delta_{32} = 0$ and $\gamma = 0$, or more generally when the probe and control are detuned by the same amount and $\delta_- = 0$ and in the limit of vanishing ground state decoherence.

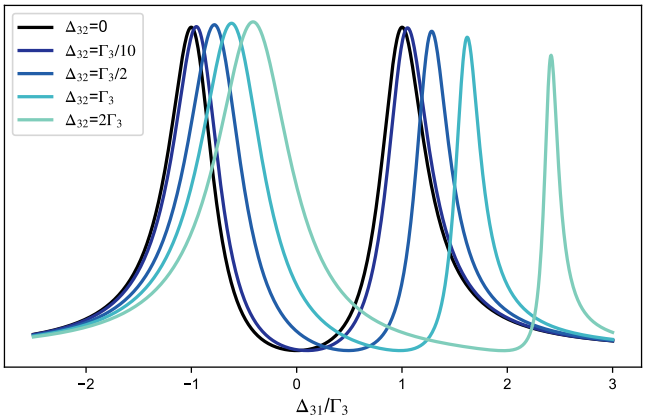

Figure 1.9: $Im[\chi_{31}]$ for the three level Λ scheme with $\Omega_{21} = \Gamma_3/10$, $\Omega_{32} = \Gamma_3$ and $\gamma = \Gamma/100$. $Im[\chi_{31}]$ vanishes when $\Delta_{21} = \Delta_{32}$ resulting in an absorption coefficient of zero for the probe beam. The narrow peak at increased Δ_{32} is the result of simultaneous absorption of a probe and meter photon.

Figure 1.9 shows the susceptibility of the probe in the Λ scheme when its frequency is swept for a fixed detuning of the control. At far control detuning, there is a single-photon absorption feature close to probe resonance that is shifted by the AC Stark shift. As the detuning of the probe approaches the control's detuning, the susceptibility goes to zero as expected, but a little past this point is another peak in absorption. This peak represents the simultaneous absorption of a probe photon and stimulated emission by a control photon, which moves an atom from $|1\rangle$ to $|2\rangle$. As the detuning of the control approaches zero, the two-photon peak broadens and becomes more symmetric with the single-photon peak. This is the regime of EIT, where nearly resonant probe light has very low absorption while still experiencing nonlinear effects from being so close to atomic resonance.

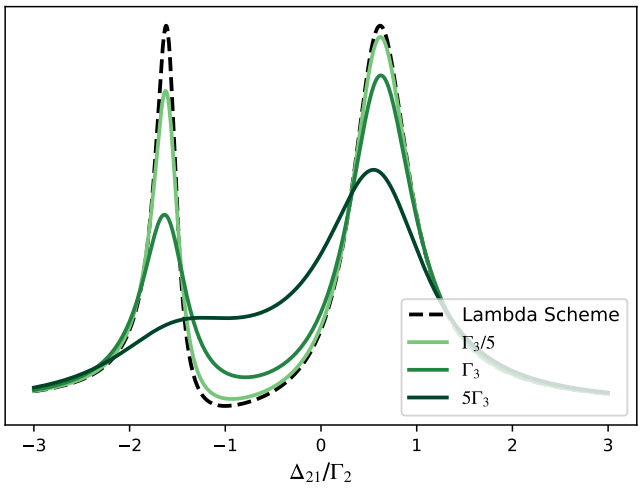

Figure 1.10: $Im[\chi_{21}]$ for the three level cascade scheme from Figure 1.6 with $\Omega_{21} = \Gamma_2/10$, $\Omega_{32} = \Gamma_2$ and $\Delta_{32} = \Gamma_{21}$. The dashed black line is $Im[\chi_{21}]$ for the Λ scheme with the same meter and probe beam powers and $\Delta_{32} = -\Gamma_2$. In the cascade scheme, because Γ_3 is generally not negligible, the dark state has a decay rate which, even in the ideal limit, reduces the induced transparency. This can be seen by the increase in $Im[\chi_{21}]$ at $\Delta_{21} = -\Delta_{32}$ as Γ_3 increases.

The analogous result to Eq. 1.47 in the cascade scheme is the c_2 equation in Eq. 1.39, since for low probe power $\rho_{21} \approx c_2$. These two equations are identical after substituting δ_- for δ_+ and setting Γ_3, in the cascade scheme, to zero. The main difference is that while setting Γ_2 to zero in the Λ scheme is usually valid, Γ_3 is certainly not going to be small and its contribution cannot be ignored. It effect is to add a decay channel to the cascade

scheme's dark state, which is the dressed state of the zero energy eigenvalue found last section,

$$|D\rangle = \frac{\Omega_{32}|1\rangle - \Omega_{21}|3\rangle}{\sqrt{\Omega_{32}^2 + \Omega_{21}^2}}, \tag{1.48}$$

that allows the atom to interact with the field again and reduces the effect of EIT. This can be seen in Figure 1.10, where it is clear that this reduction is not enough to completely negate EIT for expected atomic decay rates. The other difference is that the condition for the two-photon detuning being zero in the cascade scheme is $\Delta_{21} = -\Delta_{32}$, instead of $\Delta_{31} = \Delta_{32}$ for the Λ scheme.

1.7 Slow Light

The phenomena of slow light has been the subject of much interest over the past few decades, fueled by the incredible demonstration of group velocities as low as 17m/s in 1999 by [12]. In the context of the techniques discussed in this thesis, there are two effects of slow light that are important to consider besides the actual decrease in a pulses group velocity. The first is that this decrease in group velocity changes the shape a pulse entering a media. The reason for this is that as the front end of a pulse enters an area where it has a reduced group velocity, the back end will quickly catch up before it's slowed as well. If a pulse in air has a length t in time, its length in space will be ct outside a slowing media and $v_g t$ in it. Note it's length in time is the same inside and outside the media. This is critical to consider when discussing the overlap of two pulses in a media because if they have different group velocities, they will change length by different amounts and possibly decrease their overlap area. To complicate things further, if their group velocities are dependent on the local field strength of the other electric field, the concept of a group velocity for the pulse becomes less clear.

The other effect to consider is the creation of a propagating atomic coherence that stores some of the energy of the field. Slow light that arises from photonic crystal geometries [15] have enhanced fields that preserve the total energy of the pulse, so that if a pulse's group velocity is slowed to v_g, its intensity is increased by a factor of c/v_g. Slow light resulting from atomic coherences does not have an amplified intensity because it shares its energy with a polariton that propagates with the pulse [9]. In fact this polariton is the dark state discussed earlier, and it is possible to utilize EIT to control the velocity of this electric field-dark stat polariton pair and the ratio of energy between them [4].

For the purposes of this thesis, slow light has only a small effect, but further developments in the techniques discussed here will require a much better understanding of the role

it plays. As mentioned, when the group velocities of two pulses depend on the strength of the other pulse, cross couplings between the fields greatly complicate the picture. Work has been started on tackling this problem analytically and numerically, but in this thesis only a limiting case, absent of cross couplings will be considered.

Chapter 2

Effective Photon-Photon Interactions

The basic theory outlined above will now be applied to predict the strength of two light matter interactions. The first is phase modulation, where a weak beam of light imparts a phase shift on a much stronger beam. The second is the simultaneous absorption of photons from two lasers. To evaluate the advantages of using cold atoms over warm, the predictions will be compared to the results of similar experiments that used warm atoms.

Recent work, described in *Phase modulation at the few-photon level for weak-nonlinearity-base quantum computing* [27] and *Few-photon all-optical modulation in a photonic band-gap fiber* [28], has explored interactions between laser beams, mediated by atoms, in hollow core photonic crystal fiber. The experiments were preformed using a 9cm long hollow-core fiber (AIR-6-800, NKT Photonics) inside a vacuum chamber at 85^oC equipped with a Rubidium source. A highly non-resonant $805nm$, $3mW$ vapor generating beam was coupled into the fiber to produce optical depths around 100. The relevant energy levels of Rubidium were the three level ladder scheme $5S_{1/2} \rightarrow 5P_{3/2} \rightarrow 5D_{5/2}$, which required a 780.2nm beam for the $5S_{1/2} \rightarrow 5P_{3/2}$ transition and a 776nm beam for the $5P_{3/2} \rightarrow 5D_{5/2}$ transition. These beams were coupled into the fiber at opposite ends, so that they were counter-propagating. Atoms with velocities parallel to the beams propagation directions see Doppler shifted frequencies, and because the beams are counter-propagating the shifts of the two beams are in opposite directions. So while a traveling atom may see an off resonant beam Doppler shifted closer to resonance, the other beam will be shifted farther from resonance, resulting in a suppression of two photon processes. The consequence of this arrangement is that the only population of atoms that see both beams close to their actual frequencies are those with small velocity components parallel to the beams propagation directions, and so two photon spectral fetures are not Doppler broadened.

In *Phase modulation at the few-photon level*, the phase of the $776nm$ light was changed due to the index of refraction of atoms in the fiber, which was modified by the $780.2nm$ light through the Kerr effect. These lasers will be referred to as the meter and probe beams, respectively.The key result of *Phase modulation at the few-photon level* was found by measuring the phase shift imparted on a 10μW meter beam by a probe beam at powers ranging from one to five nanowatts. For the $5ns$ long square pulses used, this corresponds to about 10 to 100 probe photons per pulse. The relationship between meter beam phase shift and probe power is linear, and the slope of this relationship corresponds to the phase shift induced per probe photon. In *Phase modulation at the few-photon level* a .3 miliradian phase shift per probe photon was observed.

The experiment described in *Few-photon all-optical modulation* consisted of modulating the transmission of a $776nm$ beam through the atom cloud in the fiber in the presence of a $780.2nm$ beam. The power of both beams was very low, ($\sim 100pW$) and it was observed that through two photon absorption, less than 20 photons could modulate the transmission of a comparably powerfully beam by $\sim 25\%$.

2.1 Cross Phase Modulation

For CW lasers, the phase imparted on the meter by the probe is calculated in the following way. In the weak probe field limit, the atoms' first excited state has a very small population, and absorption of the meter beam is negligible. The meter beam is modelled as a plane wave traveling through a region with susceptibility χ_{32}, which is a function of the meter and probe's respective detuning and power. The equation for the meter field in the medium is

$$\begin{aligned} E_m(z,t) &= \mathcal{E}_m Exp[-ink_m(z-ct)] \\ &= \mathcal{E}_m Exp[-ik_m(z-ct)]Exp[-i\frac{k_m}{2}Re[\chi_{32}](z-ct)] \end{aligned} \tag{2.1}$$

where Eq. 1.22 has been used to replace the index of refraction with susceptibility. The phase imparted on the meter at a given z is then

$$\theta(z) = -\frac{k_p}{2}Re[\chi_{32}(z)]. \tag{2.2}$$

Here the spatial dependence of χ_{32} is due to the absorption of the probe as it propagates. The real part of χ_{32} is given by

$$Re[\chi_{32}] = \frac{N\mu_{32}^2}{\epsilon_0\hbar}\frac{\Omega_{21}^2\delta_+}{(\Delta_{21}^2+\Gamma_2^2/4)(\delta_+^2+\Gamma_3^2/4)+\Omega_{32}^4-2\Omega_{32}^2(\Delta_{21}\delta_+ + \Gamma_2\Gamma_3/4).}. \tag{2.3}$$

In order to find the total phase shift of the meter as it passes through the portion of the medium effected by the probe, the explicit dependence of χ_{32} on z must be found. The only term in Eq. 2.3 that is spatially dependent is the Ω_{21}^2 in the numerator, which is related to the magnitude of the probe field by $\Omega_{21}^2 = |\frac{\mu_{21}E_p}{\hbar}|^2$. With absorption coefficient α_{21} defined by $\alpha_{21} = k_{21}Im[\chi_{21}]$, probe electric field can be written as $E_p(z) = \mathcal{E}_p Exp[-\alpha_{21}z/2]$ and the initial intensity is

$$I_p = P_p/A = \frac{1}{2}\epsilon_0 c n_{21}|\mathcal{E}_p|^2 \tag{2.4}$$

where P_p is the initial power of the probe, A is the cross sectional area of the hollow core fiber, and n_{21} is the index of refraction of the medium with respect to the probe, which in the weak field limit is approximately one. Combining all of this gives the expression for phase shift at a particular position z and probe power P_p as

$$\theta(z) = -\frac{N k_m \mu_{32}^2 \mu_{21}^2}{c\epsilon_0^2\hbar^3}\frac{P_p}{A}\frac{\delta_+ e^{-\alpha_{21}z}}{(\Delta_{21}^2 + \Gamma_2^2/4)(\delta_+^2 + \Gamma_3^2/4) + \Omega_{32}^4 - 2\Omega_{32}^2(\Delta_{21}\delta_+ + \Gamma_2\Gamma_3/4)}. \tag{2.5}$$

The total phase shift imparted on the meter can be calculated from Eq. 2.5 as

$$\Delta\theta = \int_0^L \theta(z)\partial z = \theta_0 \int_0^L e^{-\alpha_{21}z}\partial z = \theta_0 L_{eff} \tag{2.6}$$

where θ_0 is the spatially independent part of Eq. 2.5, and L_{eff} is the effective length of the medium defined

$$L_{eff} = \frac{1 - e^{-\alpha_{21}L}}{\alpha_{21}}. \tag{2.7}$$

The physical meaning of L_{eff} is that if the probe beam was not absorbed and remained at its initial power while propagating through a cloud of length L_{eff}, then there would be the same amount of probe power in the cloud as there is in the actual physical scenario, and it would have the same effect on the meter beam.

The results of these equations will now be explored, with all constants used given in Appendix A, and the python code used for calculation given in Appendix D. The maximum phase shift imparted on the meter beam occurs when the one and two photon detunings are equal, which is illustrated in Figure 2.1, where L_{eff} and θ_0 are plotted alongside the phase shift. For $\Delta_{21} = \delta_+$, the increased transparency at the EIT window around $\Delta_{21} = 0$ coincides with relatively large values of θ_0. As $|\Delta_{32}|$ increases, the peak in θ_0 becomes narrower, and more localized to the region of very small L_{eff}. This both decreases the maximum phase shift possible, and narrows the width of the phase shift peak. At large $|\Delta_{32}|$, the large and small peaks in θ_0 are a result of the one and two photon resonance

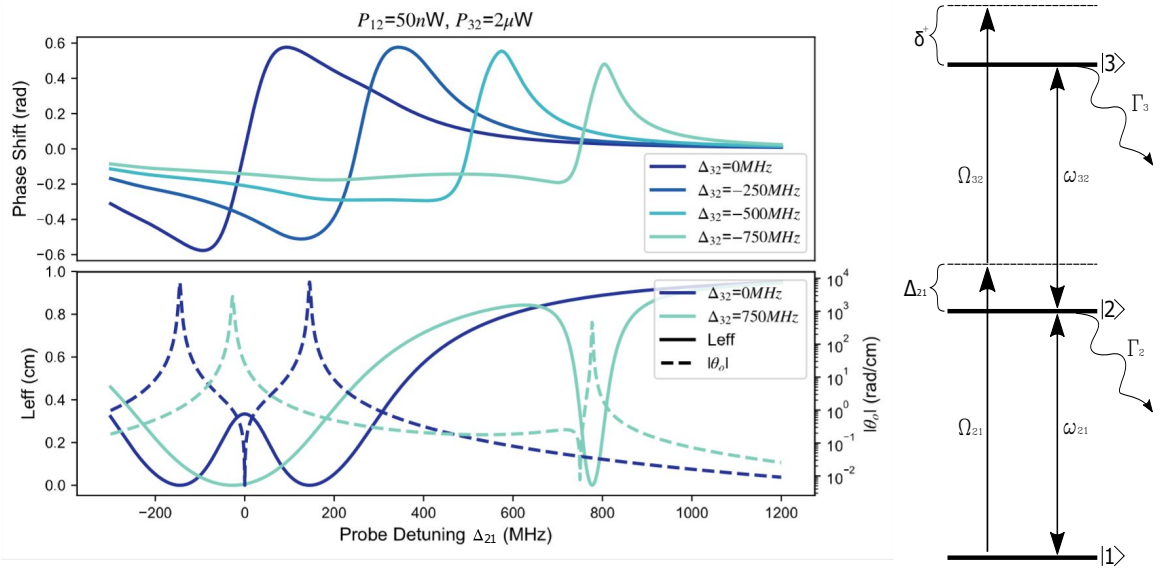

Figure 2.1: (Right)Phase shift, L_{eff}, and $|\theta_0|$ at several two photon detunings, a $50nW$ probe beam and a $2\mu W$ meter beam. It can be seen from the plots that the ideal detuning of the meter beam is $\Delta_{32} = 0$, and because $\delta_+ = \Delta_{32} + \Delta_{21}$, the ideal two photon detuning is $\delta_+ = \Delta_{21}$. Decreasing δ_+ results in less overlap of the region of non-negligible L_{eff} and $|\theta_0|$. Increasing δ_+ instead of decreasing it produces the same curves mirrored on the X and Y axes. Calculations made for a $1cm$ long cloud of cold atoms with $OD = 100$. (Left) Three level cascade scheme used for cross phase modulation experiment.

respectively. The contribution to θ_0 between these two resonances add, which leads to an increased region of θ_0 relative to the other sides of the peaks, and results in the asymmetry of the phase shift that can be clearly seen in the $\Delta_{32} = -500MHz$ and $\Delta_{32} = -750MHz$ curves of Figure 2.1. To maximize phase shift, all future predictions will be made for $\Delta_{21} = \delta_+$.

The phase shift calculation for warm atoms described in *Phase modulation at the few-photon level* was used to compare the predicted phase shift produced by cold atoms to those produced by warm atoms, the results of which can be seen in Figure 2.2. The linewidth of the two-photon resonance in warm atoms was measured by the group to be around $50MHz$ [28], and it was necessary to keep $\Delta_{21} >> 50MHz$ to avoid loss due to absorption that outweighed the increase in $Re[\chi_{32}]$ near the two-photon resonance. A long range absorption coefficient was used in Eq. 2.7, defined as

$$\alpha_{warm} = ODe^{-\frac{\Delta_{21}^2}{\omega_d^2}} \tag{2.8}$$

for an optical depth of OD and Doppler width $\omega_d \approx 300MHz$. The top right plot in Figure 2.2 shows that Ł$_{eff}$ for warm atoms approaches the actual length of the cloud more quickly than Ł$_{eff}$ for cold atoms at large Δ_{21}, but also decreases much more quickly as Δ_{21} decreases.

It was observed by Gaeta et al. that the peak phase shift occurred around $700MHz$, a prediction that is seen in the bottom right plot of Figure 2.2. The peak phase shift for cold atoms occurs at a much smaller single photon detuning, and is about an order of magnitude larger. Having a non-negligible L_{eff} at smaller probe beam detunings means that the strong light-matter interactions that occur close to the two-photon resonance can be used to enhance the phase shift. It is noteworthy that for a given optical depth, the warm atom model predicts a larger phase shift at large detunings than the cold atom model. This is because a larger atomic density is needed in warm atoms to produce the same optical depth, and at large detunings where absorption is negligible, this results in a larger phase shift.

Figure 2.3 shows how the phase shift of the meter scales with probe power, the relationship that gives the important metric of how much phase shift is imparted per probe photon. In *Phase modulation at the few-photon level*, for a $5ns$ probe pulse and a $10\mu W$ meter beam passing through a $10cm$ long cloud of warm atoms at an optical depth of ~ 100, a phase shift per photon of 0.3 miliradians was observed. For a $1cm$ long cloud of cold atoms at an optical depth of ~ 100, photons in a $5ns$ time period are prediction to impart a phase shift of .23 miliradians per photon on a $10\mu W$ meter beam. Such similar phase shift per photon for an order of magnitude shorter cloud is a clear improvement,

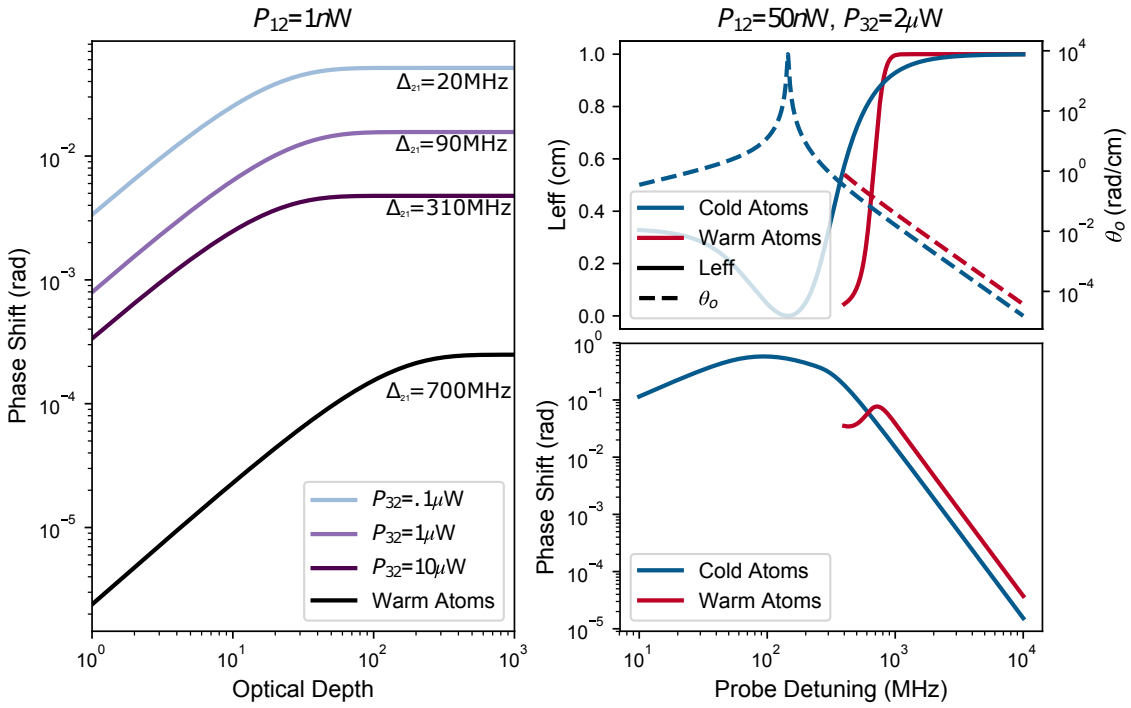

Figure 2.2: (Left) Maximum phase shift as a function of optical depth for warm atoms and cold atoms at several meter beam powers, for a $1nW$ probe beam, or equivalently a probe beam containing, on average, 4.29 photons ever nanosecond. The phase shift saturates around $OD = 20$ for cold atoms and $OD = 200$ for warm atoms. Curves are labeled with their single photon detuning.(Right) Phase shift, L_{eff} and θ_0 for cold and warm atoms with a $50nW$ probe beam and a $2\mu W$ meter beam. The curve for warm atoms has been plotted for the single photon detunings where the theory is valid, $\Delta_{21} >> 50MHz$. Calculations made for a $1cm$ cloud of atoms. The temperature of the cloud is $1mK$ for cold atoms, and $350K$ for warm atoms. Plots on the right are made for $OD = 100$.

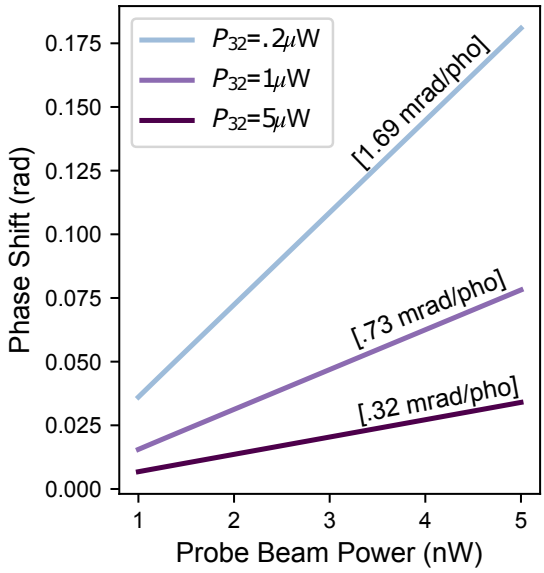

Figure 2.3: Maximum phase shift as a function of probe beam power for several meter beam powers. The slope of this relationship corresponds to the phase shift imparted on the meter beam per probe photon. Each line is labeled with it's phase shift per photon in units of miliradians per photon, assuming the power corresponds to number of photons every $5ns$. Calculation done for a $1cm$ cloud of cold atoms with $OD = 100$.

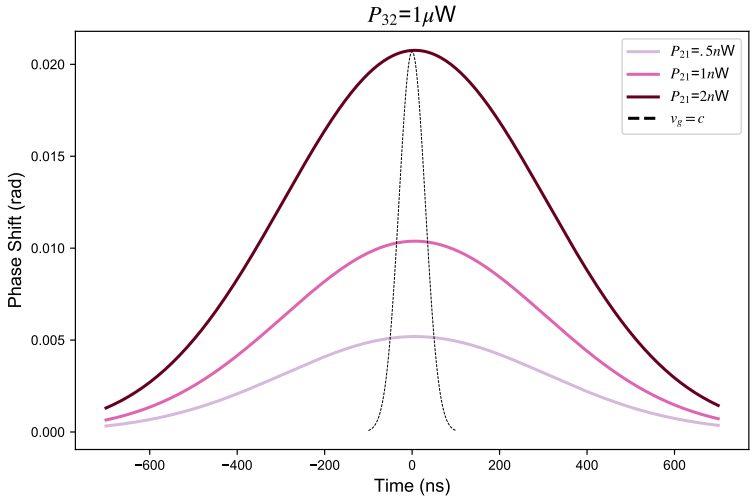

Figure 2.4: The phase imparted on a meter beam over the course of time it takes a probe pulse with FWHM=1μs to propagate through the cold atom cloud for several probe powers. The dashed line is the phase shift for the hypothetical, non-physical case where the group velocity of the probe is not changed, and is plotted to show how the lowered group velocity of the probe effects the phase shift of the meter. Calculations made for a $1cm$ cloud of cold atoms at $OD = 100$.

especially since for any practicable application of this technology, component size will be important. In addition to this improvement, in the large detunings where the warm atom model is valid, the phase shift is largely independent of meter beam power. This is not the case for the maximum phase shifts from cold atoms, and Figure 2.3 shows that further improvements to the phase shift per photon can be had at lower meter beam powers, with an order of magnitude improvement for a $0.1\mu W$ meter beam. The phase shift's sensitivity to meter beam power is a result of two factors. First, the maximum value of θ_0 increases as the meter beam power decreases, as can be seen from the inverse powers of Ω_{32} in Eq. 2.5. Second, at lower meter beam powers, larger L_{eff} values are closer to the maximum values of θ_0.

Further development of the cross phase modulation model will require considerations for pulsed beams to be made. This can prove extremely challenging in some cases, but here the next simplest case to continuous waves will be examined: continuous meter beam and pulsed probe beam. This case is simple because in the weak field limit of the probe, the power of the meter beam is not effected by absorption. Therefore, the susceptibility of the medium as seen by the probe does not vary spatially, and Eq. 1.26 and 1.27 can

be used to describe the electric field of the probe at a given time. The phase shift on a wavefront of the meter beam entering the medium at that time can then be calculated by replacing the exponentially decaying envelope $e^{-\alpha_{21}z}$ in Eq. 2.5 with the envelope found from Eq. 1.26 for the purposes of the integration done in Eq. 2.6. The result of this is the phase shift on a wavefront of the meter beam that enters the cloud at a specific time. As each wavefront enters the cloud, the probe pulse that determines its phase will have propagated and been absorbed some since the last moment, resulting in a time dependent phase shift on the meter. It is important to note that this assumes the electric field of the probe does not change appreciably as a given wavefront of the meter travels through it, but this is a valid assumption when the group velocity of the probe beam is much smaller than the speed of light, as is the case for any relevant powers and detunings.

Figure 2.4 shows the phase shift on the meter beam as a function of time for a Gaussian pulse probe beam with a full width half max (FWHM) of one microsecond. That is, Figure 2.4 shows how the measured phase shift on the probe would change over time, as the probe pulse propagates through the cloud. The dashed curve represents the hypothetical, non-physical scenario where the group velocity of the probe is not slowed. It is plotted to illustrate the effect slow light would have on this measurement. Because the probe pulse is slowed in the atomic medium, a larger section of the meter beam is effected by the induced phase shift, as it remains in the cloud for longer.

2.2 Two Photon Absorption

The measurement parameter that indicates the rate two photon absorption in the cascade scheme is the intensity of the meter beam transmitted through the cloud of cold cesium atoms. This is because absorption of the meter beam only occurs when an atom has already absorbed a probe photon and is in the first excited state. Analyzing two photon absorption can then be formulated as calculating the transmitted meter beam intensity, and starts with examining the Fourier Transform of Eq. 1.16 for the probe and the meter beam

$$\begin{aligned} \frac{\partial \mathcal{E}_p}{\partial z} &= \frac{i\omega}{2}\mathcal{E}_p + \frac{ik}{2}\chi_{21}\mathcal{E}_p \\ \frac{\partial \mathcal{E}_m}{\partial z} &= \frac{i\omega}{2}\mathcal{E}_m + \frac{ik}{2}\chi_{32}\mathcal{E}_m. \end{aligned} \tag{2.9}$$

These coupled differential equations will be solved in low power limit of both the probe and the meter, as opposed to only the probe as in the cross phase modulation case.

The first step will be to apply this low power limit to χ_{21} and χ_{32} in order to simplify the equations and allow for an analytic solution. The new parameters

$$\begin{aligned} D_1 &= \Delta_{21} + i\frac{\Gamma_2}{2} \\ D_2 &= \delta_+ + i\frac{\Gamma_3}{2}, \end{aligned} \tag{2.10}$$

will be used to increase legibility. The relevant density matrix elements can be expressed in this new notation as

$$\begin{aligned} \rho_{21} &= \frac{-\Omega_{21} D_2 (D_1^* D_2^* - \Omega_{32}^2)}{|D_1|^2|D_2|^2 + \Omega_{32}^4 - 2\Omega_{32}^2 Re[D_1 D_2^*]} \\ \rho_{32} &= \frac{-\Omega_{32}\Omega_{21}^2 D_2^*}{|D_1|^2|D_2|^2 + \Omega_{32}^4 - 2\Omega_{32}^2 Re[D_1 D_2^*]}, \end{aligned} \tag{2.11}$$

To simplify this clunky denominator, it can be expanded in the limit of $\Omega_{32} << |D_1|, |D_2|$ as

$$\begin{aligned} [|D_1|^2|D_2|^2 + \Omega_{32}^4 - 2\Omega_{32}^2 Re[D_1 D_2^*]]^{-1} \approx \\ \frac{1}{|D_1|^2|D_2|^2} + \frac{2\Omega_{32}^2 Re[D_1 D_2^*]}{|D_1|^4|D_2|^4} + \mathcal{O}(\Omega_{32}^3) \end{aligned} \tag{2.12}$$

The term of order Ω_{32}^2 can be dropped from this under the assumption that $\Omega_{32}^2 Re[D_1 D_2^*] << |D_1|^4|D_2|^4$. Removing the Ω_{32} dependence from the denominator of Eq. 2.12 allows for the susceptibilities to be written with linear dependences on squares of the fields,

$$\chi_{21} \approx -\frac{N\mu_{21}^2}{\epsilon_0 \hbar} \frac{D_2 (D_1^* D_2^* - \frac{\mu_{32}^2}{\hbar^2}|\mathcal{E}_m|^2)}{|D_1|^2|D_2|^2} \tag{2.13}$$

$$\chi_{32} \approx -\frac{N\mu_{32}^2\mu_{21}^2}{\epsilon_0 \hbar^3} \frac{|\mathcal{E}_p|^2 D_2^*}{|D_1|^2|D_2|^2} \tag{2.14}$$

greatly simplifying the coupled differential equations for the beam's intensities. To find these equations for intensity,

$$\frac{\partial I}{\partial z} = \frac{1}{2}\epsilon_0 c \left(\frac{\partial \mathcal{E}}{\partial z}\mathcal{E}^* + \mathcal{E}\frac{\partial \mathcal{E}^*}{\partial z}\right) \tag{2.15}$$

was used with 2.9 and it was found that

$$\begin{aligned} \frac{\partial I_p}{\partial z} &= \alpha I_p + \beta_p I_p I_m \\ \frac{\partial I_m}{\partial z} &= \beta_m I_p I_m \end{aligned} \tag{2.16}$$

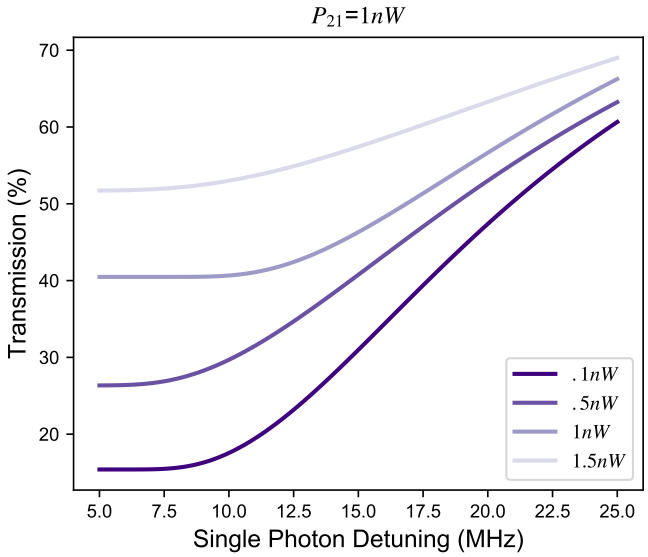

Figure 2.5: Transmission of a meter beam at several powers modulated by a $1nW$ probe beam. Calculations done for a $1cm$ long cloud of cold atoms with $OD = 100$.

where

$$\begin{aligned} \alpha &= \frac{ik_p}{2}\frac{N\mu_{21}^2}{\epsilon\hbar}\frac{(D_1^* - D_1)}{|D_1|^2} \\ \beta_j &= \frac{ik_j}{2}\frac{N\mu_{21}^2\mu_{32}^2}{\epsilon\hbar^3}\frac{(D_2^* - D_2)}{|D_1|^2|D_2|^2} \end{aligned} \tag{2.17}$$

These coupled differential equations can easily be solved numerically, but it is important to stay in a range of parameters that is consistent with assumptions made previously. This means that detunings used must satisfy $\Omega_{32}^2 Re[D_1 D_2^*] << |D_1|^4|D_2|^4$ for a given Ω_{32}, and Ω_{21} must be small enough so that $\rho_{11} \approx 1$. Along with these requirements, the differential equations were solved for $\delta_+ = 0$ because it is obvious that the maximum in two photon absorption should occur at zero two photon detuning. This was confirmed numerically.

Figure 2.5 shows the results of numerically solving Eq. 2.16 in Python for the total transmission of the meter beam at different meter beam powers. The power of the probe beam was $1nW$, which corresponds to ~ 20 photons in a $5ns$ window. In the same time window, the $1.5nW$ and $1nW$ meter beam correspond to 30 and 20 photons respectively. The curves in Figure 2.5 indicate that at these powers, the 20 probe photons can modulate

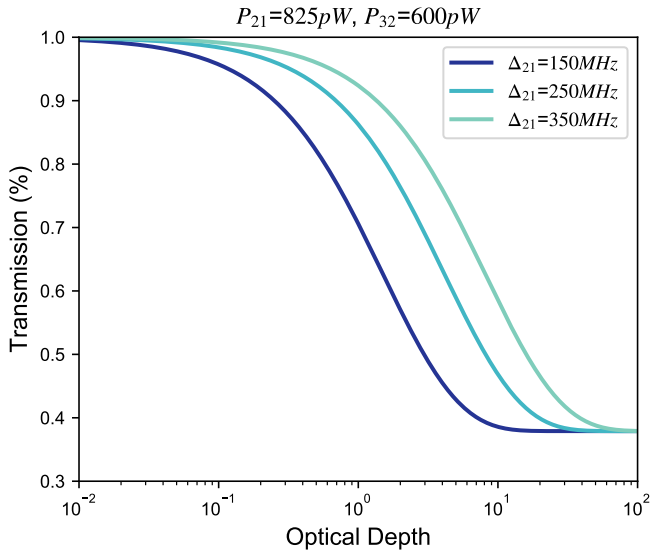

Figure 2.6: Transmission of a $600pW$ meter beam modulated by a $825pW$ probe beam for several single photon detunings, as a function of optical depth. Calculations done for a $1cm$ long cloud of cold atoms.

the transmission of almost half of 30 meter photons, and more than half for an equal number of meter photons.

In *Few-photon all-optical modulation*, it was observed that a $825pW$ probe beam could modulate the transmission of a $600pW$ meter beam by $\sim 25\%$, or in terms of photons, 16 probe photons modulating 12 meter photons, assuming $5ns$ pulse widths. To compare these results to the predictions made for cold atoms, Figure 2.6 was plotted for these beam powers, and shows that more than twice that amount of modulation can be expected when using cold atoms. Figure 2.6 also shows the effects of the single photon detuning and optical depth have on modulation rates. The $\Delta_{21} = 150MHz$ curve was near the smallest single photon detuning in which the model is valid, and the modulation amount can seen to saturate around $OD = 10$. Increasing the single photon detuning does not change the maximum modulation, but does increase the necessary optical depth needed to achieve the same modulation before saturation. This indicates that smaller single photon detunings are superior, as they require fewer atoms inside the fiber to achieve the same results.

Chapter 3

Experimental Design

The main apparatus that will be used to preform experiments consists of a HCPF mounted upright in a vacuum chamber, with an optical setup to produce a cold atom trap above the fiber. These cold atoms are loaded into the fiber, and light is coupled in from below. It interacts with the cloud of cold atoms as it falls, and is collected for measurement as it leaves the top of the chamber. The atomic levels in cesium chosen for the cascade scheme are the $6s_{1/2}, F = 4 \rightarrow 6p_{3/2}, F' = 5$ and $6p_{3/2}, F = 5 \rightarrow 8s_{1/2}, F' = 4$, the resonant wavelengths of which are $852nm$ and $794nm$ respectively. In this section, the locking scheme of the $794nm$ laser will be described, details of the experimental apparatus will be provided, and the preliminary steps towards building the measurement scheme for the phase modulation experiment will be described.

3.1 Dichroic Atomic Vapor Laser Lock

Interaction with the experimental levels requires two stably locked lasers with wavelengths at $852nm$ and $794nm$. The $852nm$ laser, which will be referred to as the probe, is provided by a Vescent Photonics distributed Bragg reflector diode laser that is locked using a saturated absorption scheme. The $794nm$ laser is provided by a extended cavity diode laser (ECDL) with variable frequency achieved by controlling the voltage across a piezo electric crystal thats length determines the angle of a Bragg grating. This laser cannot be locked in the same manner as the probe, as the corresponding atomic transition is between two excited states, not a ground and excited state. Instead, the frequency of the $794nm$ beam is monitored by measuring the transmission of the $854nm$ beam in an EIT scheme, and

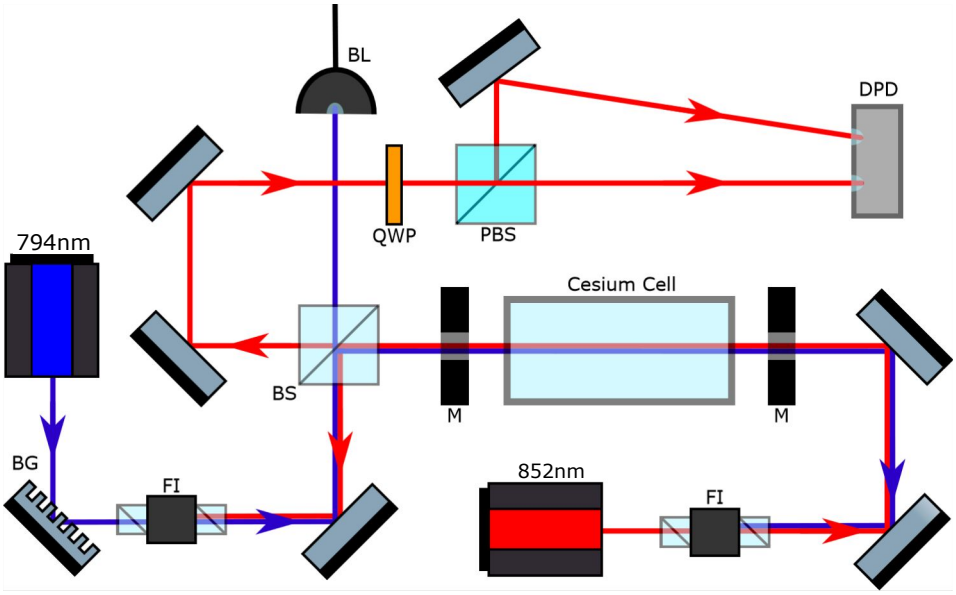

Figure 3.1: Optics scheme for EIT-based the dichroic atomic vapor laser lock. Two magnets (M) on either side of a cesium cell provide the magnetic field that breaks the degeneracy in the Zeeman levels. The component labeled DPD is a differential photo diode that's output is the difference of it's two input signals. *[Label Key:BG=Bragg Grating, BL=Beam launcher, BS=Beam Splitter, DPD=Differential photodiode, FI=Faraday Isolator, M=Magnet, PBS=Polarizing beam splitter, QWP=Quarter wave plate]*

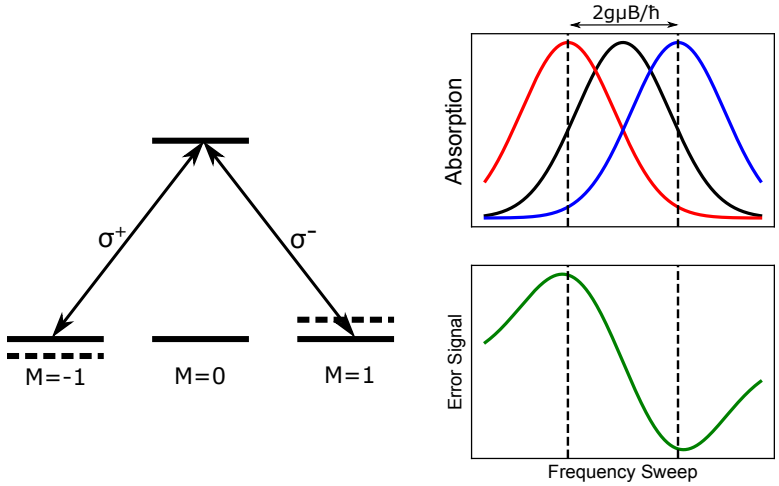

Figure 3.2: (Left) Effect of Magnetic field breaking the degeneracy of Zeeman sub-levels and the level coupling provided by the polarized light. (Right) Absorption of light in the cesium cell as the frequency is swepped through resonance. In the presence of a magnetic field, the black curve is for linearly polarized light, and the red and blue curves are for σ^+ and σ^- light, respectively. The green curve is the error signal, acquired by subtracting the blue signal from the red.

an error signal is obtained through the use of a dichroic atomic vapor laser lock (DAVLL) lock, described below. [30].

The DAVLL scheme is a locking technique that utilizes the Zeeman effect to generate an error signal that passes through zero at a desired locking wavelength. The principal of operation for a two level system is described bellow, followed by a description of how it was modified to work in a three level scheme. A schematic of the optics used in this technique is shown in Figure 3.1. The key result of a frequency stabilization scheme is the generation of a frequency error signal that passes through zero at the desired locking frequency. This is done in the DAVLL technique by utilizing the circular dichroism that arises when the Zeeman degeneracy of atoms in a vapor cell is broken by a magnetic field.

The absorption of linearly polarized light passing through a vapor cell, in the absence of a magnetic field, is a Gaussian distribution in frequency centered on resonance. This is represented as the black curve in Figure 3.2. Considering the simple case of the $F = 1 \rightarrow F' = 0$ transition, where F denotes the total angular momentum of the atom, the addition of a magnetic field with strength B will shift the energy of the Zeeman sublevels of $F = 1$ by the amount $g\mu BF/\hbar$, with Lande factor g and Bohr magneton μ, as shown in the level

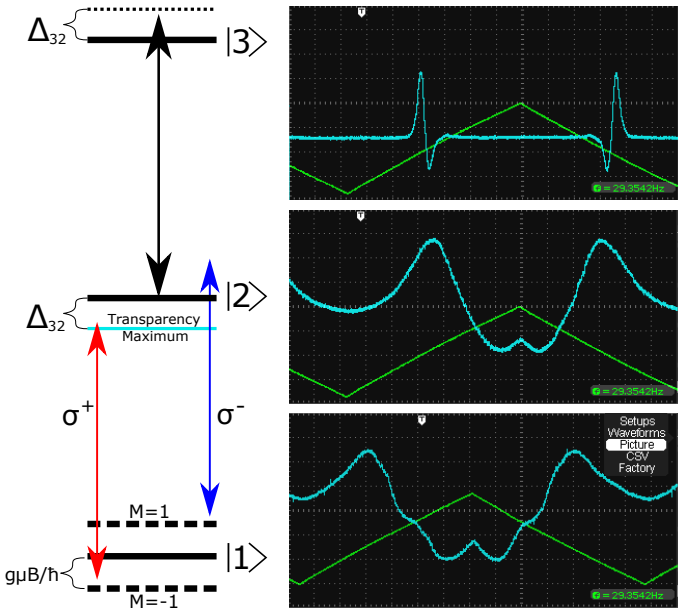

Figure 3.3: (Right) Level scheme for the DAVLL+EIT locking technique. By sweeping Δ_{32}, the transparency window provided by EIT can be scanned through the detunings of σ^+ and σ^-. Measuring the transmission of each polarization provides two offset gaussian signals, like those used in the two level DAVLL scheme, that are used to acquire an error signal crossing zero at the locking frequency. (Left Top) Blue curve is the electrical error signal resulting from subtracting one polarization transmission signal from the other. Green curve is the signal from the $794nm$ laser diode controller that represents the scan in frequency. (Left Middle) Error signal with a reduced $794nm$ frequency scanning range. (Left Bottom) Error signal resulting from an increased magnetic field across the cesium cell. The detunings of the polarizations are moved farther apart, resulting in less overlap of the gaussian transmission signals that appears as the change in the slope of the error signal.

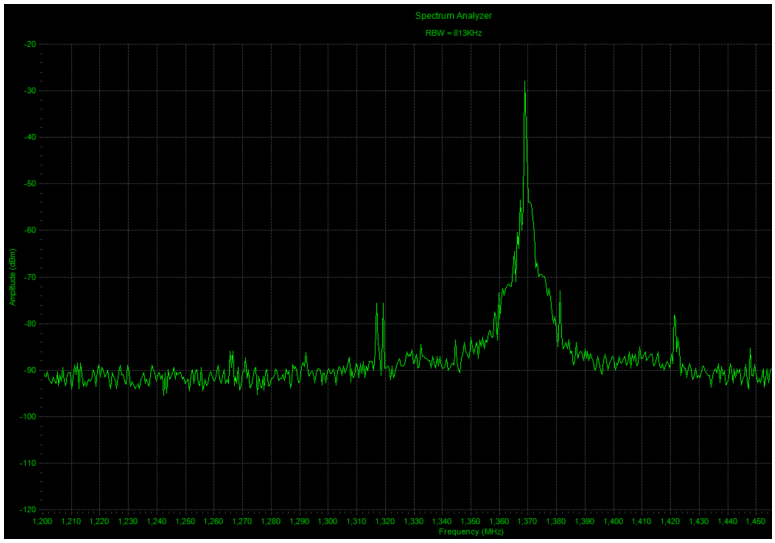

Figure 3.4: Beat note generated from locked ECDL laser and Titanium Sapphire laser tuned close to $794nm$. It appears the linewidth of the locked laser is on the order of megahertz. A noticeable difference was observed between the stability of the peak when the ECDL was locked, and when it was unlocked.

diagram of Figure 3.2. Breaking this degeneracy changes the resonance frequency of the circularly polarized components of incident light, because the Zemman sublevels $M = 1$ and $M = -1$ are shifted in opposite directions and σ^+ couples the $M = -1 \rightarrow M' = 0$ transition while σ^- couples the $M = 1 \rightarrow M' = 0$ transition. The new absorption signals of σ^- and σ^+ are sketched in Figure 3.2 as the red and blue curves, respectively. Using a $\lambda/4$ waveplate followed by a polarizing beam splitter, the circular components can be separated and measured independently with photodiodes. Subtracting one resulting electrical signal from the other produces the desired frequency error signal that passes through zero at the resonance frequency, shown as the green curve in Figure 3.2.

This scheme was adapted to lock a laser coupling the empty transition $6p_{3/2} \rightarrow 8s_{1/2}$ by utilizing the effects of EIT. Like the traditional DAVLL technique that used two level atoms, a laser driving a ground to excited state transition was sent through an atomic vapor cell and its transmission was measured. This was the $852nm$ laser, and unlike the traditional DAVLL scheme, it was already locked to resonance frequency. The $794nm$ laser was overlapped with the $852nm$ laser in the cesium cell, counterpropogating to remove the effects of Doppler broadening and allow resolution of hyperfine levels. Sweeping the $794nm$ laser through resonance would result in a Gaussian distribution in the transmission signal

of the $852nm$ laser, peaked when the $794nm$ laser was resonant. Adding a magnetic field to the cesium cell to split the Zeeman sublevels of the atoms causes the σ^- and σ^+ light to be detuned from resonance by $g\mu BF/\hbar$ and $-g\mu BF/\hbar$ respectively, as shown in Figure 3.3. Consequently, the $794nm$ laser detuning corresponding to minimum absorption of the $852nm$ light is $\Delta_{32} = -g\mu BF/\hbar$ and $\Delta_{32} = g\mu BF/\hbar$ for the respective polarizations. Separating the polarizations and measuring their intensity separately produces the two offset Gaussian signals that can be subtracted to acquire the error signal. Examples of these error signals can be seen in Figure 3.3.

A simple proportional negative feedback loop was used to adjust the voltage across the piezo crystal in the ECDL based on this error signal, and the ECDL was successfully locked to the $6p_{3/2} \rightarrow 8s_{1/2}$ line in cesium. To confirm that the ECDL was locked, a beam from a Titanium Sapphire laser was tuned close to $794nm$ and mixed with the beam from the ECDL. The beat note generated from the two beams was then measured by a spectrum analyzer, the result of which is shown in Figure 3.4. With the assumption that the linewidth of the Titanium Sapphire laser is much smaller than that of the ECDL, Figure 3.4 indicates that the linewidth of the ECDL is on the order of MHZ. It was also observed that the position of the beatnote frequency became significantly more stable when the ECDL was locked. A schematic of the locking circuit used is given in Appendix C.

3.2 Main Experimental Setup

The chamber that the cold atoms are produced in is a Cold Quanta vacuum cell, with an internal pressure on the order of 10^{-9} Torr. It contains an upright mounted HCPF segment two centimeters in length, above which the cloud of cold atoms will be formed.The cooling and trapping of cesium atoms is achieved with the use of a dual action atom trap called a magneto-optical trap (MOT). The optical component of the MOT cools atoms with three lasers shined into the vacuum cell from perpendicular directions and retro-reflected, so that any atom in motion is traveling anti-parallel with at least one beam. The light is red detuned, so that warm atoms traveling quickly see it as resonant due to the Doppler shift. The atoms then absorb light from one direction while fluorescing isotropically, which results in a decrease in velocity, as the momentum kicks from the absorbed photons accumulate and those from emitted photons average to zero. The trapping aspect of the MOT involves a magnetic field in an anti-Helmholtz configuration such that the zero point of the field is located above the HCPF. Atoms further away from this zero point will experience a proportionally larger magnetic field, causing their energy levels to be shifted further from resonance by the Zeeman shift and closer to resonance with the red detuned cooling lasers.

This causes the zero point of the magnetic field to be a potential energy minimum, so low energy atoms are confined around this region. In this way, about 10^8 cesium atoms are cooled to 120μK and trapped in the vacuum Chamber. The temperature of the atoms is then further lowered to 30μK with polarization gradient cooling, which improves loading efficiency, and are ready to be loaded into the fiber.

Using an external magnetic biasing coil, the location of the magnetic minimum in the vacuum cell can be adjusted to align the cloud of cold atoms with the HCPF. A CW TiSapph laser from MSquared produces $935nm$ beam and $\sim 40mW$ is coupled into the fiber from bellow which acts as a dipole trap for the atoms as the cooling lasers and magnetic fields are shut off. The dipole trap guides about 10^4 atoms into the core fiber, where their temperature increases to 2mK by the energy gained from falling. The temperature of the atoms in the fiber can be measured by repeatedly loading the fiber, and then turning the dipole trap off for successively increasing amounts of time, and then measuring the atom number by way of the OD. The temperature of the cloud determines the rate it disperses away from the fiber's core without the dipole trap, such that higher temperatures lead to faster decreases of OD with increasing shutoff time. The number of atoms recaptured at time τ is [3]

$$N(\tau) \approx N_o(1 - exp[\frac{-(R_{core}/r_o)^2}{1 + (v_o/r_o)^2\tau^2}]) \tag{3.1}$$

for total number of atoms N_o, fiber core radius R_{core} and beam size r_o. v_o is the most probable atomic velocity, which can also be expressed as $v_o = \sqrt{kT/m}$ for cloud temperature T, Boltzmann constant k, and mass of cesium m. By plotting the recaptured atom number vs. shutoff time and fitting it to a Eq. 3.1, v_o can be extracted, and through that, the temperature of the cloud. This measurement is shown in Figure 3.6.

With the HCPF now loaded with cold cesium atoms, the setup is ready to take a measurement for the main experiments, either cross phase modulation or two photon absorption. Now it is necessary to consider the effect of the dipole trap on the energy levels of the cesium atoms, as their shift in energy due to the AC Stark shift is not usually the same between levels. For the lambda level scheme, it is possible to choose a so called "magic wavelength" for the dipole trap that shifts all the levels in the same direction, by the same amount. However for the cascade scheme, no magic wavelength exists. As an alternative, the dipole trap must be turned off while experiments are taking place. Fortunately, time scales of the experiment are faster than the rate of dispersion of the cloud, so effects on atom numbers are small. With the dipole trap off, the experiment is performed, the cesium cloud exists the fiber, and a new MOT is formed to repeat the process. In this way, the value of experimental parameters can be swept to find the effect that parameter has on

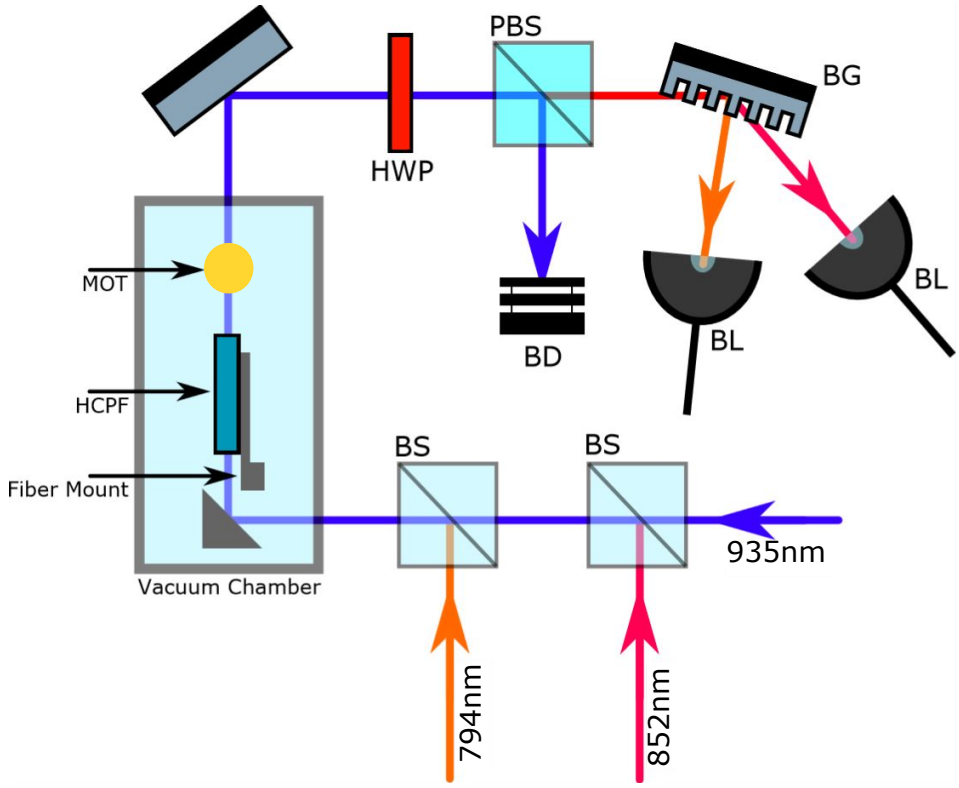

Figure 3.5: Optics setup for the main experimental apparatus. The experimental lasers and dipole trap are overlapped and coupled into the fiber from bellow with a mirror coated prism. The dipole trap is orthogonally polarized to the experimental lasers so that it can be removed with a polarizing beam splitter, while the experimental lasers will be separated with a Bragg grating. *[Label Key:BD=Beam dump, BG=Bragg Grating, BL=Beam launcher, BS=Beam Splitter, HWP=Half wave plate, PBS=Polarizing beam splitter]*

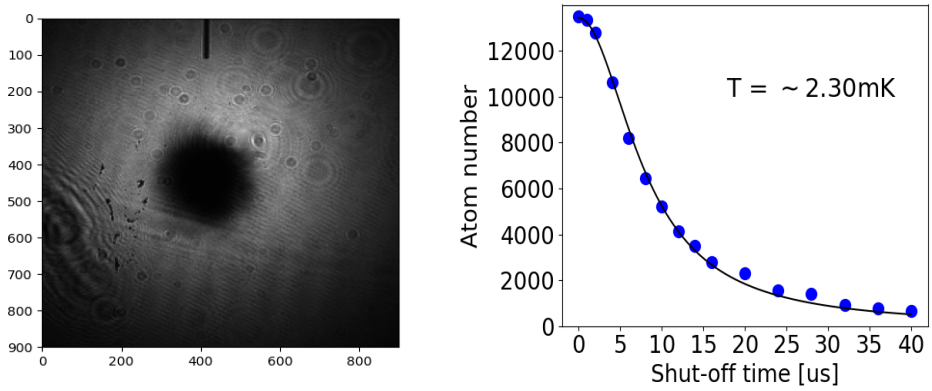

Figure 3.6: (Left) Image of MOT taken by observing the shadow the MOT casts when backlight with resonant laser light. (Right) Data collected for number of atoms re-trapped by dipole laser after a period of shutoff time. Used to calculate the temperature of atoms in the fiber. Picture and data produced by post-doctoral researcher Taehyun Yoon.

the measurement. Because new clouds of cold atoms are formed for every measurement, it is crucial that the differences between each cloud is very small.

After an experiment is performed, the light leaving the fiber is collected and must be separated by color to analyze the results of the experiment. The dipole trap is orthogonally polarized to the experimental lasers so it can be separated with a polarizing beam splitter. For experimental lasers used to probe the cascade scheme, a diffraction grating is used to separate the 852nm light from the 794nm light. Measuring the results of the two photon absorption experiment simply consists of finding the power of the transmitted 794nm light, but the cross phase modulation experiment will require the use of an interferometer to measure the phase shift.

3.3 Mach-Zehnder Interferometer

Preliminary work was begun on constructing and testing a Mach-Zehnder Interferometer for the purpose of measuring phase shifts on the order of milliradians in order to preform the phase modulation experiment. The measurement would entail splitting the meter beam in two with a 50:50 beam splitter, coupling one part into the fiber and using the other as a reference, and then recombining the beam with another 50:50 beam splitter and measuring its intensity. For a beam with initial intensity I_0 split evenly in two, the resulting intensity

I_+ or I_- obtained from measuring one of the outputs of the recombining beam splitter is

$$I_{+,-} = \frac{I_0}{2} \pm \frac{I_0}{2} cos(\phi_e - \phi_r) \tag{3.2}$$

where ϕ_e and ϕ_r are the phases of the experimental and reference beams respectively. These are given by

$$\phi_{e,r} = \frac{2\pi n_{e,r} d_{e,r}}{\lambda} \tag{3.3}$$

for average refractive index $n_{e,r}$ and path length $d_{e,r}$ of the experimental or reference paths. By adjusting the length of the reference path, the phase shift $\Delta\phi = \phi_e - \phi_r$ will be set to zero for a fiber not loaded with atoms, resulting in $I_- = 0$. Measuring the results of a phase modulation experiment would then amount to measuring the change in I_- and comparing it to Eq. 3.2 to find the phase shift $\Delta\phi$.

A test apparatus was constructed to study the stability and sensitivity of such a scheme, and to test a method of path length adjustment. This apparatus is shown in Figure 3.7. One path contained a $\sim 1cm$ segment of HCPF on a translation stage so it could be moved in or out of the path. On the other path was a retro-reflector on a translation stage that allowed the length of the path to be changed without the interferometer becoming miss-aligned. To measure the length difference between the two paths, the frequency of the laser light in the interferometer was scanned while the intensity at the output of the recombining beam splitter was measured with a photodiode. Using the relation

$$\phi_e - \phi_r = \frac{2\pi\Delta d}{c} f \tag{3.4}$$

for the path length difference $\Delta d = n_e d_e - n_r d_r$ and laser frequency f, Eq. 3.2 was fit to this data and Δd was extracted. An example of such a fit is shown in Figure 3.8, where the path length is measured to be $18.09cm$.

The results of these measurements indicated that improvements to the setup will be needed before it is capable of measuring the results of a phase modulation experiment. While it was possible to measure a difference in path length when the fiber was inserted into the path, compared to when it and the fiber coupling lenses were absent, individual measurements differed on the order of millimeters. For an average of five measurements, the path length with the fiber absent was $18.12cm$ with a standard deviation of $1.15mm$, and for the fiber present it was $18.55cm$ with a standard deviation of $1.14mm$. These results are shown in Figure 3.2. This measurement technique was used to determine the sensitivity and stability of the interferometer, and cannot be used to determine the index of refractions of the paths, and therefore of the hollow core fiber, without an accurate

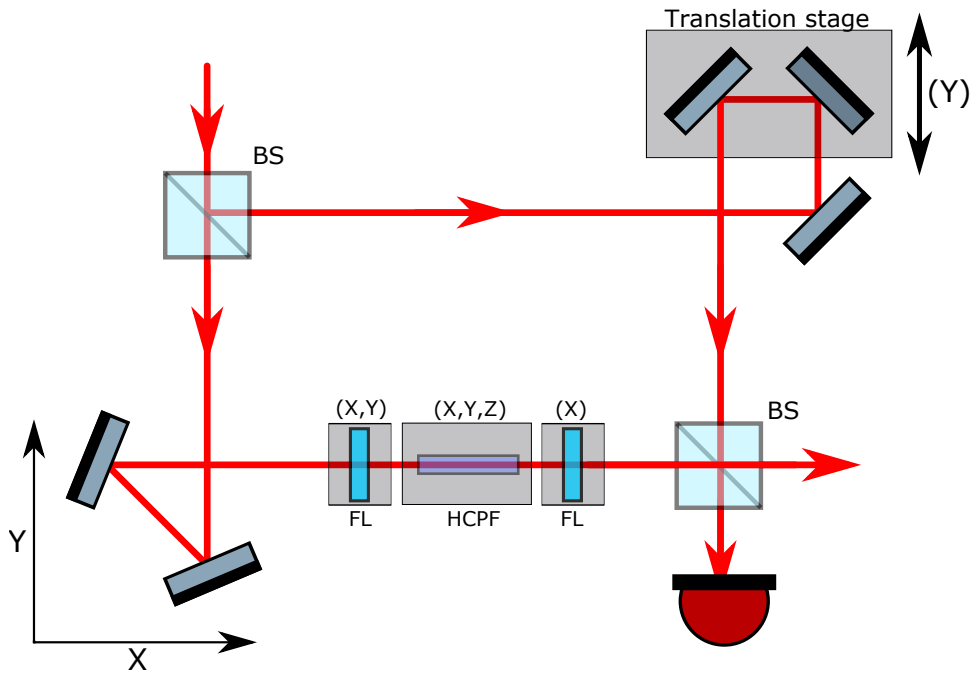

Figure 3.7: Design of the interferometer used to test the phase modulation measurement technique. One path contains a segment of HCPF that can be moved in and out of the beam, the other a retor-reflector on a translation stage to adjust the length of the path. Two $13mm$ focal length lenses (FL) were used to couple light into the fiber and then recollimate it after it exited the fiber.

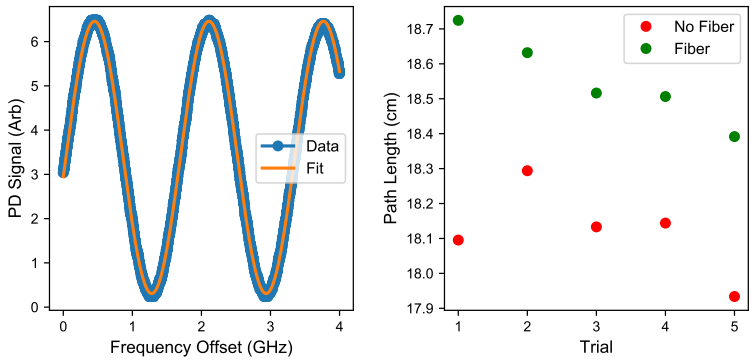

Figure 3.8: (Left) Photodiode signal as the frequency of the light in the interferometer is scanned. The frequency of oscillation obeys Eq. 3.2 and can be used to find Δd. In this fit, $\Delta d = 18.09cm$. (Right) Path length measurements for the interferometer when the HCPF was present and absent. There is a noticeable change between the two cases, but a large amount of noise is clearly present.

measurement of the physical lengths of the paths d_e and d_r. The discrepancy between measurements is likely due to noise in the system, possibly from variations in laser power, vibrations, or mechanical relaxation of optical components. For time scales on the order of $.1s$, the measured intensity signal varied by $\sim 5\%$, for $1s$ by $\sim 10\%$, and for $10s$ by upwards of 70%.

To determine the sensitivity of the interferometer to small adjustments in the path length, the optics were first changed to make the path lengths equal to within $10mm$, with the HCPF removed from the path. This ensured that the translation stage with the retro-reflector would be able to sweep the path length difference through $\Delta d = 0$. The idea was to make gradual adjustments to Δd while sweeping the frequency, and observe the oscillations in $I_{+,-}$. As $\Delta d \to 0$ the oscillations should disappear, as predicted by Eq. 3.2. This was not observed, in part because the noise of the system was on the order of adjustments to the path length, but also because the lasers available did not have a scanning range large enough to observe an appreciable segment of an oscillation in $I_{+,-}$. For $\Delta d = 1mm$, the period of $I_{+,-}$ is about $50GHz$, and the available scanning range of $5GHz$ was insufficient to get a data set that had a reliable and repeatable fit to Eq. 3.2. It is clear that in order for this measurement scheme to be useful, the sources of noise need be found and reduced, and the path length difference must be reliably set to zero. Work is ongoing to achieve these results.

Chapter 4

Conclusion

4.1 Summary

This work has proposed improvements on techniques for controlling photon-photon interactions mediated by a an atomic medium for use in a quantum computing scheme where light is used to carry information. The origin of these improvements is the coherent interaction between the electric fields and the atoms, the increased probability of interaction between light and matter, the narrow resonance features, and the low decoherence rates, possible only because of the low temperature of the atoms and the tight confinement provided by the HCPF.

The main results of this thesis are the following. For a phase modulation scheme, in which a weak probe beam modifies the refractive index of a cloud of atoms and in doing so imparts a phase shift on a much stronger meter beam, it was shown that the use of cold atoms allows for probe detunings close to atomic resonance to be used without prohibitively high amounts of absorption. This allows the larger refractive index changes that occur close to resonance to be used for phase modulation. It was predicted that a phase shift per probe photon of 0.2 miliradians could be achievable for beam powers at which a similar experiment using warm atoms, and an order of magnitude longer atomic cloud, saw a 0.3 miliradian shift. Such a similar phase shift for a smaller cloud is clearly an improvement. Further improvements are predicted at lower meter beam powers, and it should be possible to see a phase shift per probe photon on the order of a miliradian for a meter beam of $0.1\mu W$. For the optical modulation of a beam using two photon absorption, it was predicted that as few as 20 photons can be used to induce absorption of over half the photons in a beam of comparable power, and around half the photons in a stronger

beam of 30 photons. This indicates that over 50% of the photons in the first 20 photon beam participate in two photon absorption. Predictions for optical modulation using cold atoms were also shown to be superior to experimental results using warm atoms. For a 16 photon beam modulating the transmission of a 12 photon beam, predictions for cold atoms indicate that a transmission drop of $\sim 60\%$ is expected, while only a $\sim 25\%$ drop was observed in warm atoms.

4.2 Future Work

The low decoherence rates provided by cold atoms, combined with the tight confinement of light and matter present in a HCPF make the setup described in this thesis an appealing environment to study coherent light-matter interactions. The interactions described so far are only two examples of this. Work is currently underway to equip the ends of the HCPF with atom permeable mirrors to turn the segment into a cavity. The mirrors are a photonic crystal constructed by etching a square lattice of holes into the surface of a thin Si_3N_4 membrane [11]. The size, shape, and spacing of the holes determines the mirror's wavelength dependent reflectively [2], and their presence allows atoms to pass into the fiber.

Adding the cavity to the apparatus opens up several new avenues to explore coherent light-matter interactions. One possibility is to use the cavity to produce superradiance, a phenomena that has recently been demonstrated in Rb atoms confined to a cavity [5]. In a standard laser, a good quality cavity confines many photons around an atomic gain medium. The photons circulate in the cavity and extract energy from the atoms, which generally are not coherent with each other. In a superradiant laser, a smaller amount of photons are confined to a lossy, or bad, cavity. The bad cavity ensures the photons circulate only a few times, and as they interact with the atoms they create a coherent atomic ensemble with alignened dipoles. The decay of the coherent state produces a burst of nearly identical photons, leading to a laser pulse with an exceptionally small linewidth, more than ten thousand times smaller than the linewidth limit assumed for standard, good cavity lasers [5]. The requirement of a bad cavity makes this an especially attractive future HCPF experiment. Developing photonic crystal mirrors with very high reflectively is still in progress, and the smaller reflectively requirements needed for superradiance mean it will be easier to make the necessary mirrors.

It could also be possible to construct an optical transistor with the HCPF cavity, such as the one recently demonstrated in *All-Optical Switch and Transistor Gated by One Stored Photon*[6]. The experimental setup and atomic level scheme used for this experiment is

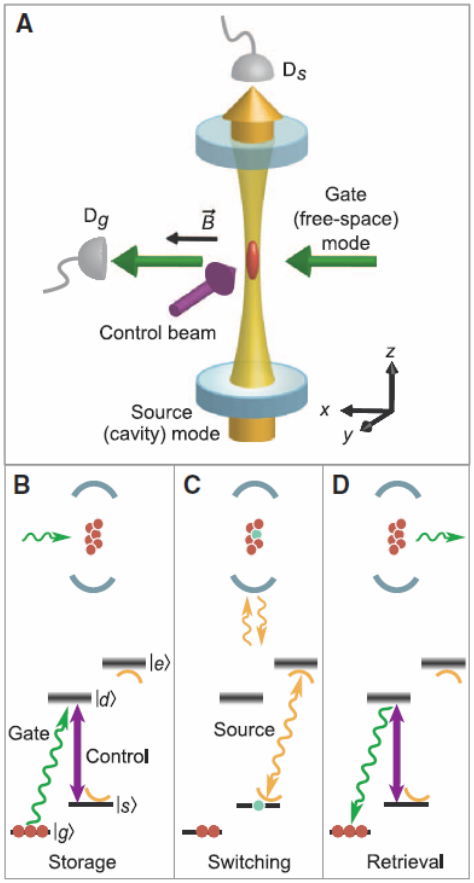

Figure 4.1: (A) Experimental setup for an optical Transistor. A cloud of cold atoms is trapped in a cavity and probed with three different lasers, a few photon gate beam, a strong control beam, and a source beam resonant with the cavity. (B) A gate pulse is stored in the atomic cloud by adiabatically reducing the control while the pulse is in the cloud, populating the $|s\rangle$ state. (C) The presence of atoms in the $|s\rangle$ state changes the resonance of the cavity, reflecting the once transmitted source beam. (D) The control is applied again, recovering the gate pulse and changing the cavity resonance back to normal. Figure acquired from *All-Optical Switch and Transistor Gated by One Stored Photon*[6]

shown in Figure 4.1. It's operation involves an N type level scheme, where a fourth energy level is added to the Λ scheme, seen in Figure 4.1 part B, and the principal of operation is as follows. A cloud of cold atoms is trapped in a cavity that's resonance frequency matches the frequency of the atom's $|s\rangle \rightarrow |e\rangle$ transition. A strong control beam coupling the $|s\rangle \rightarrow |d\rangle$ transition induces EIT for a weak gate beam coupling the $|g\rangle \rightarrow |d\rangle$ transition. By adiabatically decreasing the power of the control beam, a pulse of the gate beam can be stored in the cloud as a coherent atomic excitation [9], which populates the $|s\rangle$ state. Atoms in the $|s\rangle$ couple to the cavity, which changes its resonance frequency [26]. This causes an incident source beam that would otherwise be transmitted to be reflected. The result is that a gate pulse at the single photon level can be used to control wheather a much stronger source beam is transmitted or reflected through the cavity, and it is even possible to retrieve the gate photon by adiabatically increasing the control to reestablish EIT.

One feature of the scheme used in *All-Optical Switch and Transistor* is that it necessitates beams incident from at least two directions, as the cavity would block transmission of all but the source beam. Using a HCPF equipped with photonic crystal mirrors would make this scheme more compact. Using elliptically shaped holes, it is possible to make mirrors that have high reflectivities only for a specific polarization [2]. The three beams could then all be co-propagating, the source with a different polarization for which the mirrors have a high reflectivity.

In addition to these useful devices, employing a more advanced theoretical treatment would allow predictions to be made concerning the propagation of pulses experiencing reduced group velocities. As it stands, predicting interactions between two pulsed beams coupled via the atomic medium is extremely challenging, both analytically and numerically. But from the improvements in control of effective photon-photon interactions predicted thus far, it seems likely that advanced theoretical models could reveal even more interesting and exciting physics.

References

[1] Rubayet Al Maruf and Michal Bajcsy. On-chip splicer for coupling light between photonic crystal and solid-core fibers. *Applied optics*, 56(16):4680–4684, 2017.

[2] Amir Arbabi, Yu Horie, Mahmood Bagheri, and Andrei Faraon. Dielectric metasurfaces for complete control of phase and polarization with subwavelength spatial resolution and high transmission. *Nature nanotechnology*, 10(11):937, 2015.

[3] Michal Bajcsy, S Hofferberth, Thibault Peyronel, Vlatko Balic, Qiangrong Liang, AS Zibrov, Vladan Vuletic, and Mikhail D Lukin. Laser-cooled atoms inside a hollow-core photonic-crystal fiber. *Physical Review A*, 83(6):063830, 2011.

[4] Michal Bajcsy, Sebastian Hofferberth, Vlatko Balic, Thibault Peyronel, Mohammad Hafezi, Alexander S Zibrov, Vladan Vuletic, and Mikhail D Lukin. Efficient all-optical switching using slow light within a hollow fiber. *Physical review letters*, 102(20):203902, 2009.

[5] Justin G Bohnet, Zilong Chen, Joshua M Weiner, Dominic Meiser, Murray J Holland, and James K Thompson. A steady-state superradiant laser with less than one intracavity photon. *Nature*, 484(7392):78, 2012.

[6] Wenlan Chen, Kristin M Beck, Robert Bücker, Michael Gullans, Mikhail D Lukin, Haruka Tanji-Suzuki, and Vladan Vuletić. All-optical switch and transistor gated by one stored photon. *Science*, page 1237242, 2013.

[7] E Cojocaru. Simple expressions for gaussian-beam-waist parameters imaged by a thick lens. *Applied optics*, 34(13):2336–2338, 1995.

[8] RF Cregan, BJ Mangan, JC Knight, TA Birks, P St J Russell, PJ Roberts, and DC Allan. Single-mode photonic band gap guidance of light in air. *science*, 285(5433):1537–1539, 1999.

[9] Michael Fleischhauer and Mikhail D Lukin. Dark-state polaritons in electromagnetically induced transparency. *Physical Review Letters*, 84(22):5094, 2000.

[10] JD Franson, BC Jacobs, and TB Pittman. Quantum computing using single photons and the zeno effect. *Physical Review A*, 70(6):062302, 2004.

[11] CM Haapamaki, J Flannery, G Bappi, R Al Maruf, SV Bhaskara, O Alshehri, T Yoon, and M Bajcsy. Mesoscale cavities in hollow-core waveguides for quantum optics with atomic ensembles. *Nanophotonics*, 5(3):392–408, 2016.

[12] Lene Vestergaard Hau, Stephen E Harris, Zachary Dutton, and Cyrus H Behroozi. Light speed reduction to 17 metres per second in an ultracold atomic gas. *Nature*, 397(6720):594, 1999.

[13] BC Jacobs, TB Pittman, and JD Franson. Single photon source using laser pulses and two-photon absorption. *Physical Review A*, 74(1):010303, 2006.

[14] Bryan C Jacobs and JD Franson. All-optical switching using the quantum zeno effect and two-photon absorption. *Physical Review A*, 79(6):063830, 2009.

[15] Thomas F Krauss. Slow light in photonic crystal waveguides. *Journal of Physics D: Applied Physics*, 40(9):2666, 2007.

[16] Mikhail Lukin. Lecture notes quantum mechanics and atomic physics review, February 2005.

[17] Evan J Lunt, Bin Wu, Jared M Keeley, Philip Measor, Holger Schmidt, and Aaron R Hawkins. Hollow arrow waveguides on self-aligned pedestals for improved geometry and transmission. *IEEE Photonics Technology Letters*, 22(15):1147–1149, 2010.

[18] Peter J Mohr, Barry N Taylor, and David B Newell. Codata recommended values of the fundamental physical constants: 2010. *Journal of Physical and Chemical Reference Data*, 84(4):1527, 2012.

[19] William J Munro, Kae Nemoto, and Timothy P Spiller. Weak nonlinearities: a new route to optical quantum computation. *New Journal of Physics*, 7(1):137, 2005.

[20] N Nawi, BY Majlis, MA Mahdi, RM De La Rue, M Lonĉar, and AR Md Zain. Enhancement and reproducibility of high quality factor, one-dimensional photonic crystal/photonic wire (1d phc/phw) microcavities. *Journal of the European Optical Society-Rapid Publications*, 14(1):6, 2018.

[21] Aaron D Slepkov, Amar R Bhagwat, Vivek Venkataraman, Pablo Londero, and Alexander L Gaeta. Spectroscopy of rb atoms in hollow-core fibers. *Physical Review A*, 81(5):053825, 2010.

[22] Timothy P Spiller, Kae Nemoto, Samuel L Braunstein, William J Munro, Peter van Loock, and Gerard J Milburn. Quantum computation by communication. *New Journal of Physics*, 8(2):30, 2006.

[23] Daniel A Steck. Cesium d line data, 2003.

[24] Daniel A Steck. Classical and modern optics. *course notes available online at http://steck. us/teaching*, 2006.

[25] Daniel A Steck. Quantum and atom optics. *Oregon Center for Optics and Department of Physics, University of Oregon*, 47, 2007.

[26] RJ Thompson, G Rempe, and HJ Kimble. Observation of normal-mode splitting for an atom in an optical cavity. *Physical Review Letters*, 68(8):1132, 1992.

[27] Vivek Venkataraman, Kasturi Saha, and Alexander L Gaeta. Phase modulation at the few-photon level for weak-nonlinearity-based quantum computing. *Nature Photonics*, 7(2):138, 2013.

[28] Vivek Venkataraman, Kasturi Saha, Pablo Londero, and Alexander L Gaeta. Few-photon all-optical modulation in a photonic band-gap fiber. *Physical review letters*, 107(19):193902, 2011.

[29] Baodong Yang, Jiangyan Zhao, Tiancai Zhang, and Junmin Wang. Improvement of the spectra signal-to-noise ratio of caesium 6p3/2–8s1/2 transition and its application in laser frequency stabilization. *Journal of Physics D: Applied Physics*, 42(8):085111, 2009.

[30] Valeriy Yashchuk, Dmitry Budker, and John Davis. Laser frequency stabilization using linear magneto-optics: Technical notes. *REPORT LBNL-43523, June, Berkeley, California*, 1999.

[31] DD Yavuz. All-optical femtosecond switch using two-photon absorption. *Physical Review A*, 74(5):053804, 2006.

Appendix A

Physical Constants

Physical constants used for calculation are listed in this section.

Table A.1: General Physical Constants

Constant	Symbol	Value	Units	Source
Speed of light	c	299792458	ms^{-1}	[18]
Vacuum Permittivity	ϵ_0	$8.854187817 \times 10^{-12}$	Fm^{-1}	[18]
Plank's Constant	$\hbar$	$1.054571726 \times 10^{-34}$	Js	[18]
Boltzmann's Constant	k	$1.3806488 \times 10^{-23}$	JK^{-1}	[18]
Bohr Magneton	μ_b	$927.400968 \times 10^{-26}$	JT^{-1}	[18]
Cesium Mass	m	$2.206948457 \times 10^{-25}$	kg	[18]

Table A.2: $6^2S_{1/2} \rightarrow 6^2P_{3/2}$ Transition

Constant	Symbol	Value	Units	Source
Frequency	ω_1	$2\pi 351.72571850$	THz	[23]
Wavelength	λ_1	852.34727582	nm	[23]
$6^2P_{3/2}$ Decay Rate	Γ_2	$2\pi 5.2227$	MHz	[23]
Transition Dipole	μ_{21}	3.7971×10^{-29}	Cm	[23]

Table A.3: $6^2P_{3/2} \rightarrow 8^2S_{1/2}$ Transition

Constant	Symbol	Value	Units	Source
Frequency	ω_2	$2\pi 377.3$	THz	[29]
Wavelength	λ_2	794.6	nm	[29]
$8^2S_{1/2}$ Decay Rate	Γ_3	$2\pi 2.18$	MHz	[29]
Transition Dipole	μ_{32}	1.103×10^{-29}	Cm	[23]

Appendix B

Lens Tipped Fibers

With the current experimental setup, the coupling efficiency of light into the HCPF is less than 30%, which is achieved by placing the fiber at the focal point of light focused through a lens outside the vacuum chamber. The focal length of this lens is $18mm$, and it is limited by the fact that it must remain outside the chamber and so cannot be shorter. This is detrimental to coupling efficiency, because large focal lengths result in larger spot sizes, which results in light lost in the cladding of the fiber. A possible solution to this problem that was explored is the fabrication of optical fibers tipped with lenses that could be placed in the vacuum chamber, hundreds of micrometers away from the HCPF. Light coupled into these fibers would be focused immediately upon exiting the fiber. Below is a description of the fabrication procedures designed to make these fibers, the theoretical prediction's regarding their optical properties, and the results of measurements using the fibers.

Lenses were formed on the tips of optical fibers through the use of a calibration feature of a Orienteck T40 fiber splicer. The splicer works by sending an electrical charge through the ends of two fibers pressed together, briefly melting the glass and forming one continuous length of fiber. It's calibrating feature melted ends of two fibers that were not pressed together, and measured the distance between the resulting glass bulbs. By varying the power of the electrical discharge, it was possible to form surfaces with different curvatures. Figure B.1 shows the resulting curvatures for a range of electrical current strengths.

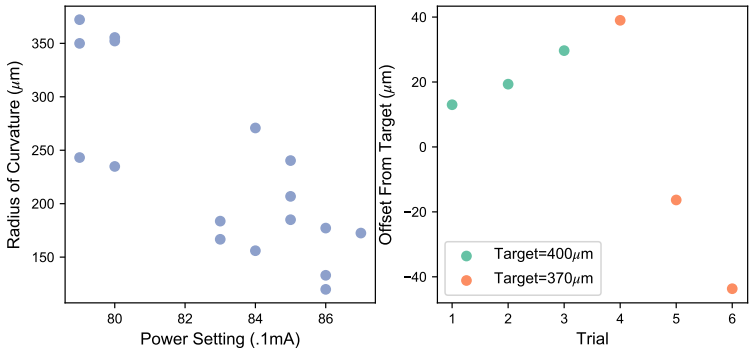

Figure B.1: (Left) Lens radius of curvature resulting from different settings of the beam splicer. (Right) Difference between the actual length of NCF spliced to a CF and the intended length. Two target lengths were used, $400\mu m$ and $370\mu m$.

A diagram of the fiber tipped lens, along with a picture of a fabricated one, is shown in figure B.2. The lens was actually formed on a segment of no-core fiber (NCF) spliced onto the cored fiber (CF). This was done to allow the beam diameter to expand some after leaving the guiding core, making a larger range of focal distances possible. The procedure to splice a precise length of NCF onto the CF was as follows. A segment of NCF was first spliced onto a CF, and the fiber was mounted on a translation stage and placed in a fiber cleaver. Using a microscope, the blade of the cleaver was aligned with the CF-NCF splice line. At this point, the translation stage was moved a precise amount to cleave the NCF, producing a CF tipped with a desired length of NC. The lengths of NCF spliced onto the CF we're within $\sim 40\mu m$ of the target length, as shown by several trials in figure B.1.

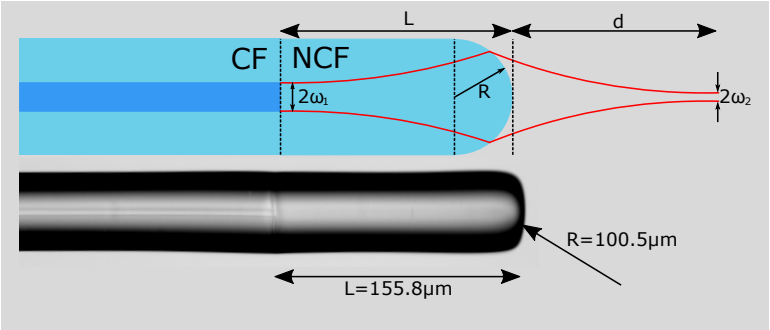

Figure B.2: (Top) Diagram of lens tipped fiber. A segment of core-less fiber (NCF) of length L is spliced onto a cored fiber (CF) and then melted to form a lens with radius R. The beam radius leaving the core is $\omega_1 = 2.75\mu m$ and has a minimum radius ω_2 after traveling a distance d from the fiber tip. (Bottom) Microscope image of the fabricated lens tipped fiber for which the focal length and beam waist was measured.

To predict the focal length and spot size for a given length of NCF and radius of lens tip, the ABCD Law described in [24] was used. This method uses the elements of the propagation matrix for optical components to determine the geometry of a Gaussian beam passing through those components. A propagation matrix of the form

$$M = \begin{bmatrix} A & B \\ C & D \end{bmatrix}, \tag{B.1}$$

has elements

$$\begin{aligned} A &= 1 - \frac{nd}{f} \\ B &= d - \frac{L}{n} + \frac{Ld}{f} \\ C &= -\frac{n}{f} \\ D &= 1 + \frac{L}{f} \end{aligned} \tag{B.2}$$

for a NCF tipped with a lens [7]. The parameters of these elements are a length of NCF segment L, an image distance d, an index of refraction $n \approx 1.52$, and an equivalent focal distance f given by

$$f = \frac{nR}{n-1} \tag{B.3}$$

where R is the lenses radius of curvature.

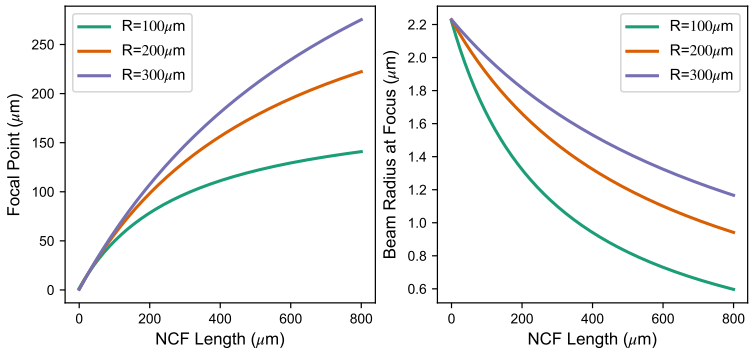

Figure B.3: Calculation predictions for the focal point distance from fiber tip and the radius of the beam at the focal point for several radii of curvature as a function of NCF.

The geometry of a Gaussian beam can be summarized by the complex parameter $q(z)$ defined

$$q(z) = z - iz_o \tag{B.4}$$

for a distance from beam waist minimum z and Rayleigh length z_o. The Rayleigh length is related to the radius of the beam at its minimum, called ω_o, by

$$z_o = \frac{\pi\omega_o^2}{\lambda}. \tag{B.5}$$

The inverse of $q(z)$ is

$$\frac{1}{q(z)} = \frac{1}{R(z)} + \frac{i\lambda}{\pi\omega_o^2(z)}, \tag{B.6}$$

where $R(z)$ is the beam's radius of curvature at point z and $\omega_o(z)$ is the beam waist defined as

$$\omega(z) = \omega_o\sqrt{1 + \frac{z}{z_o}^2}. \tag{B.7}$$

If the q parameter for a Gaussian beam incident on an optical system is q_1, then the parameter for the beam transformed by the optics, q_2, can be found from

$$\frac{1}{q_2} = \frac{C + D/q_1}{A + B/q1}. \tag{B.8}$$

To find the location of the minimum beam size, Eq. B.8 is compared to Eq. B.6 at the beam waist minimum $z = 0$. The radius of curvature of the beam is infinite here,

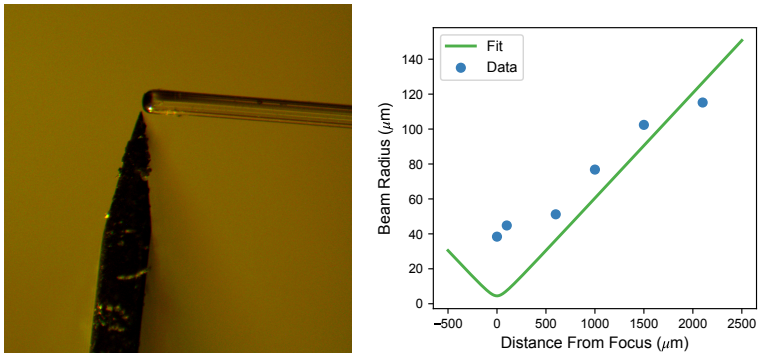

Figure B.4: (Left) Microscope picture of razor blade used to measure focal distance and beam radius with the fiber. (Right) Measured beam radius with fit to Eq. B.7. The fit predicts a minimum beam radius of $4.5\mu m$, but the measured value is closer to $40\mu m$.

so $\frac{1}{R(0)} \to 0$, implying that the real part of Eq. B.8 is vanishes. Separating the real and imaginary parts of Eq. B.8 for $q_1(0) = -iz_o$ results in

$$\frac{1}{q_2(0)} = \frac{BD + ACz_o^2 + iz_o(AD - BD)}{A^2 Z_o^2 + B^2}. \tag{B.9}$$

Applying the matrix elements defined in Eq. B.2 and solving for d, the distance from the fiber tip, gives the location of the focal point as

$$d = \frac{\frac{n}{f}z_o^2 + \frac{L}{n} + \frac{L^2}{nf}}{(1 + \frac{L}{f})^2 + (\frac{n}{f}z_o)^2}. \tag{B.10}$$

The imaginary part of Eq. B.9 can then be used to find the beam radius at this point by solving for w_o in terms of the elements of M,

$$w_o = \sqrt{\frac{\lambda}{\pi}\frac{A^2 z_o^2 + B^2}{z_o(AD - BC)}}, \tag{B.11}$$

and plugging in d from Eq. B.10. Figure B.3 shows the result of these predictions as the length of NCF is increased and for different lens curvatures. Plots go up to NCF lengths of $800\mu m$ because Eq. B.7 predicts that past this length, the width of the beam will be the same and the width of the NCF.

Once a lens tipped fiber was fabricated, it was necessary to measure the location of the focus and its minimum spot size. To find the focus, light was coupled into the fiber

and the output spot from the lens was observed on IR detecting paper. A razor blade was mounted on a translation stage and placed so the blade was perpendicular to the fiber, as shown in the microscope image in figure C.2. The blade was moved into the path of the beam while the spot was observed. If the shadow of the blade appeared on the same side of the cut, the blade was past the focal point. If it appeared on the opposite side, the blade was before the focal point. If the blade was at the focal point, the shadow would appear symmetrically on both sides of the spot. Using the microscope to measure the distance of the blade from the fiber tip at this point provided a measurement of the focal point location.

Of the fiber lenses fabricated, only one had an identifiable focal point. It is possible that the focal point of the other fibers was too close to the fiber tip compared to the width of the blade, and it couldn't cut the beam without moving the fiber. This failure in design could be a result of the fabrication process that led to fairly unpredictable results for the length of NCF and lens radius of curvature. Especially the lens radius of curvature, as the results of the melting process varied between trials by as much as $100\mu m$, and in some cases by much more. Most of the fabricated fibers had unintentionally small focal distances, which was probably exacerbated by the aspheric shape of the lenses resulting in less clearly defined focal points.

The functioning fiber lens is shown in the microscope image of figure B.2. The length of its NCF region was $155.8\mu m$, and its radius of curvature was $100.5\mu m$, predicting a focal distance d of $67\mu m$. The measured value of d was $110\mu m$. The discrepancy may be due to the aspheric lens shape. The spot size was measured with the razor blade in the following way. The intensity profile of a Gaussian beam propagating in the z direction is

$$I(x,y) = I_o e^{-x^2/\omega_x^2} e^{-y^2/\omega_y^2}, \tag{B.12}$$

where ω_x and ω_y are $1/e$ widths of the beam, defined as the beam radius, in the x and y directions. This can be integrated over all space to find the total power, but if the beam is blocked up till a point x_o, such that the intensity is zero for all y values when $x < x_o$, the total measured power is

$$P(x_o) = \frac{P_{tot}}{2}(1 - erf(\sqrt{2}x_o/\omega_x), \tag{B.13}$$

where erf is the error function and P_{tot} is the total, unblocked beam power. The value of x_o where 10% of the power is blocked is $X_{10} = -.64\omega_x$, and for 90% of the power it is $X_{90} = .64\omega_x$. Thus, if the razor blade is set to block 10% of the total beam power, and then moved to the point where it blocks 90% of the beam power, the distance it moved

can be used to find ω_x through the relation

$$X_{90} - X_{10} = 1.28\omega_x. \tag{B.14}$$

This measurement method was used to find the beam radius at several z values past the focal point, and then fit to Eq. B.7 to find the minimum radius w_o, as shown in figure C.2. The value of w_o found was $4.5\mu m$, though the measured data shows a much larger minimum beam radius, again most likely due to an aspheric lens. For a perfectly spherical lens, the expected minimum beam radius is $1.45\mu m$.

The conclusion of these tests were that this may not be the best method to improve coupling efficiency to the HCPF. Difficult and uncertain fabrication processes made making consistent samples unlikely, and the aspheric lens shapes had a negative effect on the final result. This is not a problem with an easy solution, as there is little control in the formation of the lenses. Another route that is being explored is butt coupling a solid core fiber to the hollow core fiber with a fabricated, on-chip coupler [1].

Appendix C

Laser Locking Circuit

The circuit used to lock the $794nm$ ECDL is shown in figure C.1. The outputs of the differential photodiode is input to the signal - and signal + nodes where they are subtracted to produce the error signal. This signal is added to a variable +12V DC voltage so that the offset of the error signal can be controlled and the locking section of the error signal can be made to pass through zero at the appropriate point. The signal then passes through a variable amplifier to control the strength of the feedback. Then, the signal is inverted, which is necessary for a negative feedback loop due to the polarization of the piezoelectric crystal in the diode. The signal leaves the circuit after this, and is input into the port on the ECDL control box that controls the voltage of the piezoelectric crystal.

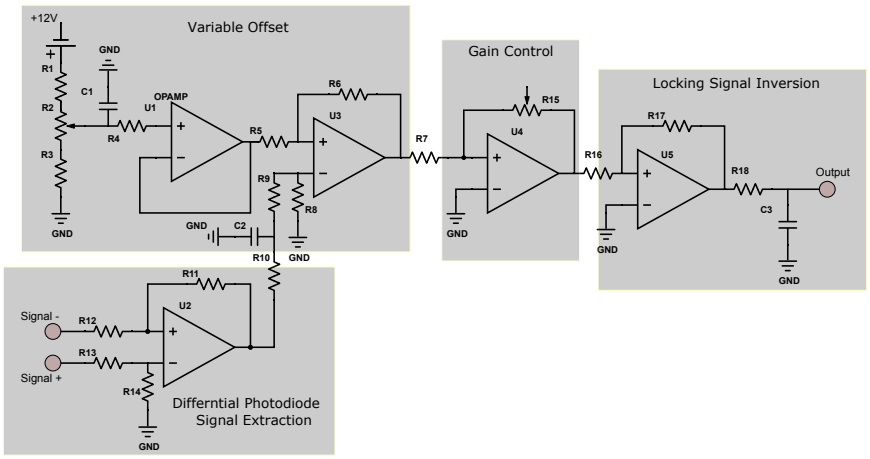

Figure C.1: Circuit used to lock ECDL in DAVLL+EIT scheme. *Op-Amp: U1-U5=TL081. Resistors: R1=12KΩ, R2=10KΩ, R3=12KΩ, R4=100KΩ, R5=8.2KΩ, R6=8.2KΩ, R7=12KΩ, R8=8.2KΩ, R9=8.2KΩ, R10=1.5KΩ, R11=18KΩ, R12=18KΩ, R13=18KΩ, R14=18KΩ, R15=100KΩ, R16=12KΩ, R17=12KΩ, R12=18KΩ. Capacitors: C1=1μF, C2=100μF, C3=10nF*

The response of the locking circuit to input signal frequency was measured, and the results can be seen in figure C.2. The Bode plot indicates that input signals with frequency larger than $1KHz$ are greatly attenuated. This is not a problem for the error signal, which changes on time scales of $\sim 100Hz$. The dependence of the phase of the output signal on the frequency of the input signal was also measured, in order to confirm that it was much less than π radians. This is important for a negative feedback loop because if the response of the loop is out of phase from the input by π radians, it can act as positive feedback. It was confirmed that the phase shift was negligible for relevant frequencies.

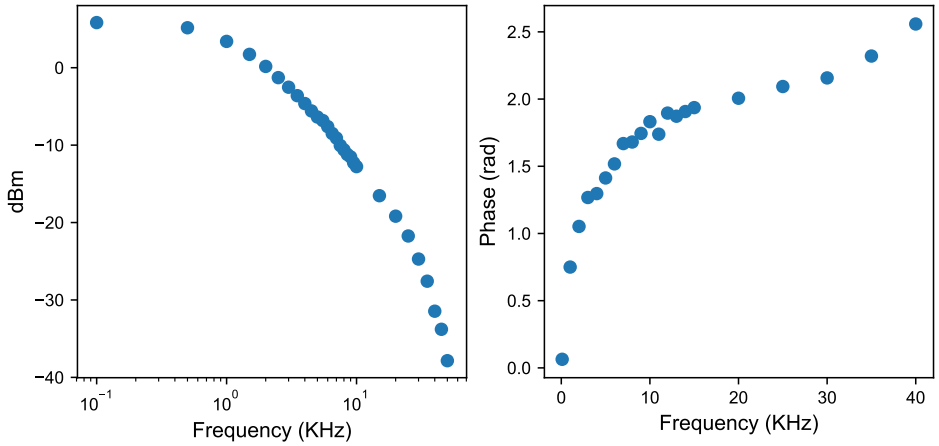

Figure C.2: Characterization of the circuit in figure C.1. (Left) Bode plot, showing a rapid dropoff in the output power as the frequency of the input signal is increased. (Right) Phase of the output signal as a function of the frequency of the input signal.

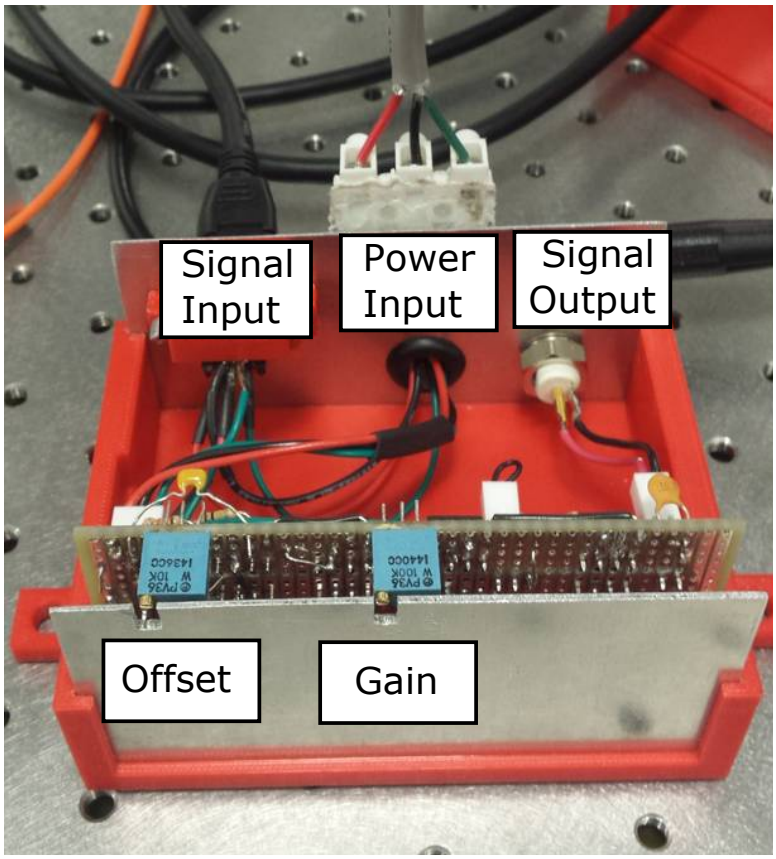

Figure C.3: Locking circuit mounted in 3D printed lockbox, with the signal input, signal output and power input cables attached. Variable resistors are placed to allow access when the box is closed.

Appendix D

Python Code

The following is a summary of the python code written to preform calculations concerning light interacting with two and three level atoms.

```
import numpy as np
import matplotlib.pyplot as plt
import matplotlib.gridspec as gridspec
from matplotlib.pyplot import rc
import matplotlib.lines as mlines
from scipy.misc import derivative
import scipy.integrate as integrate
import pylab
import scipy

c = 299792458           #Speed of light
h = 1.0545718E-34       #hbar
ep = 8.854187817E-12    #Permittivity of free space
bolt = 1.38064852E-23   #Boltzmann constant

A = 4.418E-11           #Cross sectional area of fiber
m = 2.2069468E-25       #Mass of cesium

q1 = 852E-9             #Wavelength of probe
k1 = 2*np.pi/q1         #Wavenumber of probe
w1 = c*k1               #Frequency of probe
u1 = 2.00125E-29        #Dipole strength of ground to first excited
q2 = 794.6E-9             #Wavelength of meter
k2 = 2*np.pi/q2         #Wavenumber of meter
w2 = c*k2               #frequency of meter
u2 = 8.22629E-30        #Dipole strength of first excited to second excited
den = 5E17              #Atomic density for OD=100 in cold atoms

G1 = 2*np.pi*5.22*1E6  #Decay Rate of first excited state
G2 = 2*np.pi*2.18*1E6  #Decay Rate of second excited state

c1 = (.5*A*c*ep*(h/(2*u1))**2)**-(1/2)  #Bean power to rabi frequency
c2 = (.5*A*c*ep*(h/(2*u2))**2)**-(1/2)

chi1 = den*(u1**2)/(2*ep*h)     #Density element to susceptibility
chi2 = den*(u2**2)/(2*ep*h)

```

```
37
38 #Two level atom density matrix equations
39 def two_C1(x, P):
40     part1 = -x*P + 1j*G1*P/2
41     part2 = x**2 + (G1**2)/4
42     return part1/part2
43
44 def two_p11(x, P):
45     part1 = P**2
46     part2 = x**2 + (G1/2)**2 + 2*P**2
47     return part1/part2
48
49 def two_p10(x, P):
50     part1 = -P*(x - 1j*G1/2)
51     part2 = x**2 + (G1/2)**2 + 2*P**2
52     return part1/part2
53
54 #Warm atom equations
55 def therm_dist(v, T):
56     C = np.sqrt(m/(2*np.pi*bolt*T))
57     A = m/(2*bolt*T)
58     return C*np.exp(-A*v**2)
59
60 def therm_integrand_re(v, T, x, P):
61     return therm_dist(v, T)*two_p10(x + k1*v, P).real
62
63 def therm_integrand_im(v, T, x, P):
64     return therm_dist(v, T)*two_p10(x + k1*v, P).imag
65
66 def therm_integrand_p11(v, T, x, P):
67     return therm_dist(v, T)*two_p11(x + k1*v, P).real
68
69 #Doppler broadened density elements
70 def warm_p10re(x, P, T):
71     return integrate.quad(therm_integrand_re, -np.inf, np.inf, args=(T, x, P))[0]
72
73 def warm_p10im(x, P, T):
74     return integrate.quad(therm_integrand_im, -np.inf, np.inf, args=(T, x, P))[0]
75
76 def warm_p11(x, P, T):
77     return integrate.quad(therm_integrand_p11, -np.inf, np.inf, args=(T, x, P))[0]
78
```

```
#Cold and warm cross sections and densities from OD
def CS_cold(x, P):
    I = (1/2)*c*ep*(P*h/u1)**2
    return h*w1*G1*two_p11(x, P)/I

def CS_warm(x, P, T):
    I = (1/2)*c*ep*(P*h/u1)**2
    return h*w1*G1*warm_p11(x, P, T)/I

def density_cold(x, P, OD):
    CS = CS_cold(x, P)
    return OD/(CS*.01)

def density_warm(x, P, OD, T):
    CS = CS_warm(x, P, T)
    return OD/(CS*.01)

#Three level atom density elements (cascade scheme)
def three_C1(x, y, P, M):
    num = -P*((x + y) + 1j*G2/2)
    den = (x + 1j*G1/2)*((x + y) + 1j*G2/2) - M**2
    return num/den

def three_C2(x, y, P, M):
    num = P*M
    den = (x + 1j*G1/2)*((x + y) + 1j*G2/2) - M**2
    return num/den

def p11(x, y, P, M):
    out = three_C1(x, y, P, M)
    return out*np.conjugate(out)

def p22(x, y, P, M):
    out = three_C2(x, y, P, M)
    return out*np.conjugate(out)

def p10(x, y, P, M):
    return three_C1(x, y, P, M)

def p21(x, y, P, M):
    return three_C2(x, y, P, M)*np.conjugate(three_C1(x, y, P, M))

```

```
#Three level atom density elements (lambda scheme)
def lam_C1(x, y, P, M):
    num = -P*(x - y)
    den = (x + 1j*G1/2)*(x - y) - M**2
    return num/den

def lam_C2(x, y, P, M):
    num = P*M
    den = (x + 1j*G1/2)*(x - y) - M**2
    return num/den

def lam_p10(x, y, P, M):
    return lam_C1(x, y, P, M)

def lam_p21(x, y, P, M):

    return lam_C2(x, y, P, M)*np.conjugate(lam_C1(x, y, P, M))

#Slow Light
def dp10(x, y, P, M):
    return derivative(p10, x, args=(y, P, M))

def Vg(x, y, M):
    dchi = chi1*dp10(x, y, 1, M)
    den =  1 + (c*k1/2)*dchi
    return c/den

#Cold atom effective length and phase shift, dependent on OD
def Leff_coldOD(x, y, P, M, OD):
    N = density_cold(0, P, OD)
    alpha = (k1)*(N/den)*(chi1/P)*p10(x, y, P, M).imag
    return (1 - np.exp(-alpha*1E-2))/alpha

def phase_coldOD(x, y, P, M, OD):
    N = density_cold(0, P, OD)
    L = Leff_coldOD(x, y, P, M, OD)
    P21 = (k2/2)*(N/den)*(chi2/M)*p21(x, y, P, M).real
    return P21*L

```

```
#warm atom effective length and phase shift, dependent on OD
def WLeffOD(x, L, OD):
    wd = 2*np.pi*325E6
    alpha = OD*100*np.exp(-(x/wd)**2)
    if (x/(2*np.pi*1E6)) < 1500:
        sol = (1 - np.exp(-alpha*L*1E-2))/alpha
    else:
        sol = L*1E-2
    return sol

def phase_warmOD(x, y, P, M, OD, L):
    Le = WLeffOD(x, L, OD)
    P21 = (k2/2)*(density_warm(0, P, OD, 350)/den)*(chi2/M)*p21(x, y, P, M).real
    return P21*Le

#Probe pulse shape at (z, t) and total phase shift imparted by propogating probe
def pulse(z, t, x, y, M):
    L = 1E-6
    A = 4*np.log(2)/L**2
    vg = Vg(x, y, M)
    chi = chi1*p10(x, y, 1, M)

    c1 = np.exp(1j*z*k1*chi/2)
    c2 = np.exp(-A*(t - z/vg)**2)
    out = c1*c2*np.conjugate(c1*c2)
    return out

def pulse_phase(t, x, y, P, M):
    theta = (k2/2)*(chi2/M)*p21(x, y, P, M).real
    length = integrate.quad(pulse, 0, 1E-4, args=(t, x, y, M))[0]
    return length*theta

#TPA differential equation
def coupled_intensity(y, z, alpha, beta1, beta2):
    Ip, Im = y
    C = 1
    dydz = [alpha*Ip + C*beta1*Ip*Im, C*beta2*Ip*Im]
    return dydz

```

```
#Approximations of susceptibility
def C1(x, y):
    D1 = x + 1j*G1/2
    return (np.conjugate(D1) - D1)/(D1*np.conjugate(D1))

def C2(x, y):
    D1 = x + 1j*G1/2
    D2 = x + y + 1j*G2/2
    denom = (D1*np.conjugate(D1))*(D2*np.conjugate(D2))
    return (np.conjugate(D2) - D2)/denom

#Coefficients of the coupled differential equations
def alpha(x, y):
    return (k1*den*C1(x, y)*(u1**2)/(2*ep*h)).imag

def beta1(x, y):
    return (k1*den*C2(x, y)*(u1**2)*(u2**2)/((ep**2)*c*h**3)).imag

def beta2(x, y):
    return (k2*den*C2(x, y)*(u1**2)*(u2**2)/((ep**2)*c*h**3)).imag

#Solution to differential equations
def Two_photon_abs(Zmax, x, y, P, M):
    Z = np.linspace(0, Zmax, 1000)

    initial_p = .5*c*ep*(h*P/u1)**2
    initial_m = .5*c*ep*(h*M/u2)**2
    initial = [initial_p, initial_m]

    a = alpha(x, y)
    b1 = beta1(x, y)
    b2 = beta2(x, y)

    sol = integrate.odeint(coupled_intensity, initial, Z, args=(a, b1, b2))

    IP = sol[:,0]/initial[0]
    IM = sol[:,1]/initial[1]
    return [IP, IM]

```

Appendix E

Mot Components

The following is an inventory of the optical, mechanical, and vacuum components that were used to produce a MOT in a vacuum chamber.

Name	Manufacturer	Part Number	Number of Parts	Cost	Total Cost
Feedthru	MDC	9132001	1	$227.00	$227.00
Ag Plated Bolts	Duniway Stockroom	*varies	100	$3.00	$300.00
Copper Gaskets	*varies	*varies	10	$2.50	$25.00
Glass Cell	Cold Quanta	2cm AR Coated Cell	1	$10,000.00	$10,000.00
Reducing Nipple	Nor-Cal	2NRC-338-275	1	$135.00	$135.00
Aspheric Lens	Thor Labs	354280-B	1	$78.60	$78.60
NEG Cables	SAES	3B0386, 3B0338A	1	$348.34	$348.34
Reducing Tee	Nor-Cal	3TR-200-075	1	$285.00	$285.00
Achromatic Doublet	Thor Labs	AC254-075-B	1	$111.35	$111.35
Achromatic Doublet	Thor Labs	AC254-300-B	1	$111.35	$111.35
Aspheric Lens	Thor Labs	AL2550-B	2	$299.99	$599.98
All Metal Valve	Nor-Cal	AMV-1502-CF	1	$840.00	$840.00
Mounting Base	Thor Labs	BA1S	40	$6.81	$272.48
NEG	SAES	Capacitorr D-100	1	$2,787.00	$2,787.00
NEG Power Supply	SAES	CF 35 D100	1	$1,023.00	$1,023.00
Short Clamping Fork	Thor Labs	CF125	4	$11.46	$45.85
Threaded Cage Plate	Thor Labs	CP02	2	$20.96	$41.92
Ion Pump Controller	Gamma Vacuum	Digitel SPC	1	$1,418.00	$1,418.00
Flip Mount Adaptor	Thor Labs	FM90	1	$105.19	$105.19
Optical Mount	Thor Labs	FMP1	4	$20.23	$80.91
Iris	Thor Labs	ID15	1	$60.00	$60.00
Irs	Thor Labs	ID25	3	$72.18	$216.54
Ion Gauge	Instrutech	IGM401YFD	1	$845.00	$845.00
Kinematic Mirror Mount	Thor Labs	KM100	11	$50.70	$557.67
Kinematic Platform Mount	Thor Labs	KM100B	4	$70.74	$282.96
Kinematic Prism Mount	Thor Labs	KM100PM	4	$94.98	$379.90
Threaded Kinematic Mount	Thor Labs	KM100T	1	$83.84	$83.84
Best Form Lens	Thor Labs	LBF254-050-B	1	$67.73	$67.73
Clean-Up Filter	Semrock	LL01-852-12.5	1	$305.00	$305.00

Name	Manufacturer	Part Number	Number of Parts	Cost	Total Cost
Lens Mount	Thor Labs	LMR1	1	$19.95	$19.95
Linear Polarizer	Thor Labs	LPNIRE100-B	1	$140.17	$140.17
45 Degree Mount	Thor Labs	MA45-2	3	$26.99	$80.96
Groove Grabbers	Kimball Physics	MCF275-GrvGrb-CYL0750	1	$395.00	$395.00
Spherical Cube Brackets	Kimball Physics	MCF275-MtgFlg-C2	2	$80.00	$160.00
Spherical Cube	Kimball Physics	MCF275-SphCube-C6	1	$788.00	$788.00
Reflective Filter	Thor Labs	ND20A	1	$89.53	$89.53
Reflective Filter	Thor Labs	ND30A	1	$89.53	$89.53
PBS	FOCtek	PBS1307-852	3	$55.00	$165.00
PBS	Thor Labs	PBS202	1	$259.38	$259.38
Post Holder	Thor Labs	PH1	32	$9.21	$294.70
Post Holder	Thor Labs	PH1.5	6	$9.46	$56.75
Post Holder	Thor Labs	PH2	2	$10.09	$20.17
Post Holder	Thor Labs	PH3	1	$10.83	$10.83
Fiber Optics	OZ Optics	PMJ-3A3A-850-5/125-3-10-1	4	$291.00	$1,164.00
Fiber Optics	OZ Optics	PMJ-3A3A-850-5/125-3A-3-1	1	$700.00	$700.00
Post Collar	Thor Labs	R2	1	$6.27	$6.27
Right Angle End Clamp	Thor Labs	RA180	3	$13.49	$40.48
Right Angle Clamp	Thor Labs	RA90	3	$12.79	$38.36
Pedestal Post	Thor Labs	RS1P8E	3	$27.51	$82.53
Fiber Adapter Plate	Thor Labs	SM1FCA	4	$39.30	$157.20
Stackable Lens Tubes	Thor Labs	SM1L20	1	$21.62	$21.62
Z Axis Translation Mount	Thor Labs	SM1Z	3	$243.66	$730.98
Ion Pump	Gamma Vacuum	TiTan 3S	1	$736.00	$736.00
Optical Post	Thor Labs	TR1	14	$6.21	$86.93
Optical Post	Thor Labs	TR1.5	15	$6.51	$97.66
Optical Post	Thor Labs	TR2	10	$6.80	$67.99
Optical Post	Thor Labs	TR3	4	$7.10	$28.40
Optical Post	Thor Labs	TR4	1	$7.69	$7.69
XYZ Translation Stage	unknown	unkown	2	$250.00	$500.00
Half Wave Plate	Red Optr	WPO-225H-850	3	$125.00	$375.00
Quarter Wave Plate	Red Optr	WPO-225Q-850	6	$125.00	$750.00
Electrical Coils	home built		2		
				Total	$29,795.68